Unclassified
SECURITY CLASSIFICATION OF THIS PAGE

AD-A205 649

DTIC FILE COPY

REPORT DOCUMENTATION PAGE

DTIC ELECTE MAR 27 1989 S D

1a. REPORT SECURITY CLASSIFICATION: Unclassified	1b. RESTRICTIVE MARKINGS: none
2a. SECURITY CLASSIFICATION AUTHORITY:	3. DISTRIBUTION/AVAILABILITY OF REPORT: APPROVED FOR Public Release; DISTRIBUTION Unlimited
2b. DECLASSIFICATION/DOWNGRADING SCHEDULE:	
4. PERFORMING ORGANIZATION REPORT NUMBER(S):	5. MONITORING ORGANIZATION REPORT NUMBER(S): AFOSR-TR- 89-0318
6a. NAME OF PERFORMING ORGANIZATION: Eastern Montana College	6b. OFFICE SYMBOL (If applicable):
6c. ADDRESS (City, State and ZIP Code): Dept. of Physical Sciences, 1500 North 30th Street, Billings, MT 59101-0298	7a. NAME OF MONITORING ORGANIZATION: AFOSR
	7b. ADDRESS (City, State and ZIP Code): Bolling Air Force Base, DC 20332-6448
8a. NAME OF FUNDING/SPONSORING ORGANIZATION: AFOSR	8b. OFFICE SYMBOL (If applicable): NP
	9. PROCUREMENT INSTRUMENT IDENTIFICATION NUMBER: AFOSR-85-0139
8c. ADDRESS (City, State and ZIP Code): Bolling Air Force Base, DC 20332-6448	10. SOURCE OF FUNDING NOS.

PROGRAM ELEMENT NO.	PROJECT NO.	TASK NO.	WORK UNIT NO.
61102F	2311	A1	

11. TITLE (Include Security Classification): Study of Infrared Celestial Background

12. PERSONAL AUTHOR(S): Dr. Alan F. Bentley

13a. TYPE OF REPORT	13b. TIME COVERED	14. DATE OF REPORT (Yr., Mo., Day)	15. PAGE COUNT
Final	FROM 2/1/85 TO 1/31/88	1988 Sep 30	8

16. SUPPLEMENTARY NOTATION

17. COSATI CODES			18. SUBJECT TERMS (Continue on reverse if necessary and identify by block number)
FIELD	GROUP	SUB GR.	

19. ABSTRACT (Continue on reverse if necessary and identify by block number)

During the three year period under the grant, 01 Feb 1985 to 31 Jan 1988, telescopic observations were carried out on selected infrared sources, theoretical investigations were pursued, five papers were published, a sixth had been submitted, and work was going forward at the end of the grant period on the investigation of the infrared nature of planetary nebula nuclei.

20. DISTRIBUTION/AVAILABILITY OF ABSTRACT	21. ABSTRACT SECURITY CLASSIFICATION
UNCLASSIFIED/UNLIMITED XX SAME AS RPT. ☐ DTIC USERS ☐	Unclassified

22a. NAME OF RESPONSIBLE INDIVIDUAL	22b. TELEPHONE NUMBER (Include Area Code)	22c. OFFICE SYMBOL
Dr. Henry R. Radoski	202/767-4906	NP

DD FORM 1473, 83 APR — EDITION OF 1 JAN 73 IS OBSOLETE.

Unclassified
SECURITY CLASSIFICATION OF THIS PAGE

AFOSR-TR- 89 0318

Report No._____

STUDY OF THE INFRARED CELESTIAL BACKGROUND

Alan F. Bentley
Department of Physical Sciences
Eastern Montana College
1500 North 30th Street
Billings, Montana 59101-0298

30 Sep 1988

Final Report for Period 1 February 1985 - 31 January 1988

Prepared for

AIR FORCE OFFICE OF SCIENTIFIC RESEARCH
Bolling Air Force Base, DC 20332-6448

89 3 22 084

TABLE OF CONTENTS

		Page
Abstract		3
I.	Synopsis	4
II.	Research Status	5
	A. Objectives	5
	B. Revised Objectives	5
	C. Research Progress	6
III.	Appendix	8
	A. Infrared Sources and Excitation of the W40 Complex	
	B. Radio and Infrared Observations of OH/IR Stars at the Tangential Point and Near the Galactic Center	
	C. Infrared Observations of the Early Universe	
	D. The Neon Nova. II. Condensation of Silicate Grains in the Ejecta of Nova Vulpeculae 1984 Number 2	
	E. Can Cosmic Ray Energy be Transferred Anisotropically to an Astrophysical Plasma?	
	F. A Search for Cool Companions of Planetary Nebula Nuclei	

Accesion For
NTIS CRA&I
DTIC TAB
Unannounced
Justification
By
Distribution /
Availability Codes
Dist | Avail and/or Special
A-1
QUALITY INSPECTED 4

ABSTRACT

During the three year period under the grant, 01 Feb 1985 to 31 Jan 1988, telescopic observations were carried out on selected infrared sources, theoretical investigations were pursued, five papers were published, a sixth had been submitted, and work was going forward at the end of the grant period on the investigation of the infrared nature of planetary nebula nuclei.

I. SYNOPSIS

Start date on the grant was 01 Feb 1985, but funding was not made available by AFOSR until after 15 April 1985. Computer equipment purchased with grant funds was acquired and placed in service during the summer of 1985. At the same time a student assistant, David Mikelson, was hired to assist with telescopic observations, computer programming, and data reduction.

The announcement in the fall of 1985 by AFGL that the LAIRTS program would not be funded had a major impact on the scientific program to be carried out under this grant. LAIRTS science planning was discontinued, and major emphasis was shifted to ground based infrared observing and analytical studies.

In early 1986 David Mikelson resigned from his position as assistant, and for the remainder of the contract period I was unable to recruit a qualified replacement for him from among the EMC student body. Eastern Montana College is a poorly funded state institution, which in some respects has not evolved into a true four-year college with a balanced Arts and Science curriculum, with the result that we have very few science oriented students on campus.

Purchase of IRAS data was initially postponed when it was learned that the data set would cost approximately $4000, as compared to $200 estimated in the original cost proposal. In early 1986 unexpended funds from the first year of the grant became available, and permission to use a portion of these funds for purchase of the IRAS data was requested from AFOSR. After a full six-month delay, this request was granted. By then it

had become apparent that qualified student help was not available, so I put off ordering the IRAS data until I had my student help problem solved. This never happened, so the IRAS database was never purchased.

Despite the delays and problems mentioned above, research under the grant went forward in terms of continuing scientific observations and the publication or preparation for publication of research results.

As a result of the lack of qualified student assistants on this campus, a paucity of meaningful College support for scientific endeavor, and a recent administrative decision to de-emphasize the physical sciences even further, I have regretfully decided against proposing further AFOSR grant support for my research.

II. RESEARCH STATUS

A. Objectives

The scientific objectives of this research program, as stated in the grant proposal, were:

(1) to determine the nature of infrared sources observed.

(2) to establish the statistical distribution of infrared sources in space to a sensitivity limit of 10^{-20} W cm^{-2} and a spatial resolution of 4 arcseconds.

B. Revised Objectives

Due to cancellation of the LAIRTS program by the Air Force, the following revised objectives for this research program were formulated:

(1) to determine the nature of infrared sources observed.

(2) to carry out theoretical investigations on the nature and evolution of selected infrared sources.

(3) to establish the statistical distribution of infrasources in space to a sensitivity limit and spatial resolution consistent with available observing equipment and techniques.

C. Research Progress

During the grant period, 01 Feb 1985 to 31 Jan 1988, progress toward the research objectives was made, as follows:

(1) Research on infrared sources in the W40 complex was published in the Astrophysical Journal. A copy of the paper is included in the appendix.

(2) Results of radio and infrared observations of OH/IR stars in the Galaxy were published in the Astrophysical Journal. Acopy of this paper is included in the appendix.

(3) A theoretical study of the possibilities for observation of galaxies in the process of formation in the early universe was published in the Proceedings of the Montana Academy of Science. A copy of this paper is included in the appendix.

(4) In collaboration with a number of colleagues from Wyoming, the results of a series of observations made on Nova Vulpeculae 1984 #2 were published in the Astrophysical Journal (Letters). A copy of this paper is included in the appendix.

(5) Preliminary results on our studies of the infrared properties of the nuclei of planetary nebulae were presented in Mexico City at the IAU Symposium #131 on planetary nebulae, in October 1987. An abstract of this paper is being published in the Symposium Proceedings, and a copy is included in the appendix.

(6) A theoretical model has been constructed for the transfer of cosmic ray energy to emission nebulae, and has been sent to the Astrophysical Journal for publication, and the paper has been returned, with reviewer's comments, for revision. A copy of the original draft of this paper is included in the appendix.

APPENDIX

THE ASTROPHYSICAL JOURNAL, 291:571–580, 1985 April 15
© 1985 The American Astronomical Society. All rights reserved. Printed in U.S.A.

INFRARED SOURCES AND EXCITATION OF THE W40 COMPLEX

J. SMITH, A. BENTLEY, M. CASTELAZ, R. D. GEHRZ, G. L. GRASDALEN, AND J. A. HACKWELL
Wyoming Infrared Observatory, Department of Physics and Astronomy, University of Wyoming
Received 1984 August 8; accepted 1984 October 10

ABSTRACT

Infrared images and photometry are presented for the W40 molecular cloud and H II region complex. The images, sampled through a 5" aperture and observed at effective wavelengths of 2.3, 3.6, 4.9, 10.0, and 19.5 μm, reveal only unresolved sources clustered near the peak of thermal H II emission. Six of the seven detected sources coincide with faint but optically observable stars. The photometry suggests that the three brightest sources are heavily obscured early-type stars surrounded by infrared emitting circumstellar materials. In some cases, much of the compact infrared emission may be produced by circumstellar condensations.

The three brightest sources (IRS 1a, 2a, and 3a) are candidates for producing the level of excitation inferred for both the dust and H II plasma of the W40 complex. Observed circumstellar dust has a negligible effect on the excitation of the W40 region. Instead, the predominant mode of excitation, whereby radiant luminosities of the exciting stars are absorbed by the W40 dust, appears to involve only diffuse dust mixed with the molecules, atoms and plasma.

Subject headings: infrared: sources — interstellar: matter — nebulae: H II regions — nebulae: individual

I. INTRODUCTION

W40 is an H II region and molecular cloud complex lying 3.5 above the galactic plane and approximately 700 pc from Earth. The H II region has a diameter of ~5' and a moderate emission measure of $\sim 1 \times 10^5$ pc cm^{-6} (Goss and Shaver 1970), showing that it has undergone the rapid phases of dynamical evolution normally associated with the formation and expansion of a compact H II region. Other components of the W40 complex are a 10' × 20' molecular cloud of moderate CO brightness temperature (Zeilik and Lada 1978), clouds of obscuring dust that radiate bright far-infrared and middle-infrared continua (Olthof 1974; Price and Walker 1976), and a cluster of infrared sources centered on the H II region (Zeilik and Lada 1978). Formed from these components, the W40 morphology can be described as an extensive molecular complex, the bright core of which lies in a side-by-side relationship with an evolved H II region and its sources of excitation.

In view of its distance from Earth, galactic environment, and observed morphology, the W40 complex should prove interesting for a variety of detailed studies pertinent to young stars and how they interact with their interstellar environments. For this study, we chose to concentrate on a small, ~3 arcmin^2 region centered near the position of peak H II emission. Our objective was to produce a detailed infrared study of the exciting sources of the H II region.

II. OBSERVATIONS

All measurements were made from the Wyoming Infrared Observatory (WIRO). The first step in data acquisition involved taking 64" × 64" images centered on the three bright 2.2 μm sources discovered and named IRS 1, 2, and 3 by Zeilik and Lada (1978). Each of the images was obtained using the methods described in Hackwell, Grasdalen, and Gehrz (1982) and Gehrz *et al.* (1982). For all of the observed images, including those required for the calibration stars, the sampling interval was 1" with the reference aperture positioned 60" north of the signal aperture. The aperture diameter was ~5" (FWHM).

Thermal infrared emission produced by the telescope and sky must be removed from the total signal. For the $\lambda \geq 3.6$ μm images, which were observed with a bolometer detector, this terrestrial emission was corrected with a two-step process. First, reference aperture signals were subtracted from the image signals during data acquisition at the WIRO. Later, final reduction involved removing from each image any effects of spatial gradients in detected terrestrial emission. These effects were inferred from columns of pixels forming image boundaries, along which zero celestial emission was assumed.

Unlike the $\lambda \geq 3.6$ μm images observed with the bolometer AC coupled to its preamplifier, the 2.3 μm images were observed with a photovoltaic detector coupled directly in the current integrating mode to its preamplifier and data acquisition electronics. Since reference aperture signals were not subtracted, each pixel of integrated charge represents an absolute surface brightness. Each 2.3 μm surface brightness was corrected for terrestrial emission in much the same way described above for the $\lambda \geq 3.6$ μm images.

Guided by the preliminary imaging results, we began measuring optical-infrared energy distributions of the brightest imaged sources. Infrared photometry was done with reference aperture spacings ranging from 10" to 60". For the *UBV* photometry, the sky readings were taken 20" north of each measured star. Apertures (FWHM) were 5" for the 4.9 μm, mostly 5" but occasionally 10" for the *KL*, 10" for the *JH*, and 12" for the *UBV* photometry.

We calibrated the observed 4.9 μm flux densities and also most of the 2.3 and 3.6 μm flux densities with observations of the stars μ UMa, α Lyr, β Peg, and α Boo (Gehrz, Hackwell, and Jones 1974). See Johnson *et al.* (1966) for the flux densities of σ Her and ν Cyg, observations of which calibrated the *JH* and also the remaining *K* (2.3 μm) and *L* (3.6 μm) photometry.

Positions of the infrared sources were measured by peaking up on the individual sources and recording the telescope position. Observations of the IRC +00 360, SAO 142364, and SAO 142368 positions calibrated the W40 positions (Table 1), each measured with a ±1" uncertainty.

TABLE 1

PARAMETERS OF THE INFRARED IMAGES OF FIGURE 1

	Maximum Level	Faintest Level		
$\lambda(\mu m)$	(Jy arcsec^{-2})	(mJy arcsec^{-2})	(percent)	(mag aperture^{-1})*
2.3	0.17	2.6	1.5	10.8
3.6	0.26	16	6	7.6
4.9	0.26	31	12	5.8
10	1.9	56	3	3.8
19.5	4.1	520	12	−0.2

* FWHM ≈ 5″ and area ≈ 20 arcsec^2 for the aperture

III. RESULTS

Figure 1 shows the five infrared images observed for portions of the W40 complex. Dashed lines give boundaries of the observed images ranging in size from 5 arcmin^2 for 2.3 μm down to 1 arcmin^2 for 4.9 and 19.5 μm. See the upper left corner of Figure 1*a* for representative point source responses for the photometers used to measure the images. Each response has ∼20 arcsec^2 for its integrated area and FWHM ≈ 5″. For each image, Table 1 gives the surface brightnesses corresponding to the maximum contour level of 100% and to the faintest level that was chosen to have the 3 σ statistical significance. The faintest levels are given in units of mJy arcsec^{-2}, percent of maximum surface brightness, and also magnitude per 5″ aperture.

The 2.3 μm image (Fig. 1*a*) consists of seven sources (IRS 1a, 1b, 1c, 1d, 2a, 2b, and 3a) clustered near the position of peak H II emission labeled by "H II" in Figure 1*a*. For $\lambda \geq 2.3$ μm (Figs. 1*a*–1*e*), each detected source has FWHM ≈ 5″, the size expected for a point source observed with our photometers; we find no significant evidence for extended emission at any observed wavelength. The positions of the infrared sources are given in Table 2. The positions of IRS 1a, 2a, and 3a agree with the positions given by Zeilik and Lada (1976) for IRS 1, 2, and 3.

A comparison of the 2.3 μm image with the POSS E print (Fig. 1*f*) shows that all but one (IRS 1b) of the seven infrared sources has an optical counterpart. Any optical counterpart to IRS 1b must have $R \geq 20$, the limiting magnitude of the E print. Figure 1*a* and Table 2 give the positions and names of the optical sources. Two of the compact optical sources in Table 2, OS 2c and 4a, are visible in Figure 1*f*, but we did not detect infrared counterparts. Only OS 1a, 2a, and 3a are visible on the blue POSS print.

Of the infrared observations presented in Figure 1, the 2.3 μm image has the greatest sensitivity to main-sequence stars obscured by moderate column densities of dust. The 10.5 mag limit corresponds to the 2.3 μm mag of an unobscured B5 ZAMS star located at the W40 distance of 700 pc (see below). Therefore, any main-sequence stars too faint to appear in the 2.3 μm image should contribute negligibly to the O9 V level of H II excitation inferred below for W40.

The mean surface brightness of H II continuum emission extrapolated from the radio continuum measurements of W40 (Goss and Shaver 1970, beam = 4′; Zeilik and Lada 1978, beam = 2′) is approximately 20 times smaller than the limiting 3 σ surface brightness at 2.3 μm of $\sim 2 \times 10^{-3}$ Jy arcsec^{-2}. That limit and also the small 60″ reference aperture spacing explain why Figure 1*a* shows no diffuse H II emission.

The 2.2 μm map made by Zeilik and Lada (1978) with large sizes of aperture diameter (44″) and reference aperture spacing (240″) covers approximately the same region shown in Figure 1*a*. Summing the 2.3 μm flux densities of all seven infrared sources of Figure 1*a* gives 7.1 Jy, which approximates closely the 10 ± 1 Jy (corrected slightly from 2.2 to 2.3 μm) given by Zeilik and Lada for their map. This means that any diffuse emission detected by Zeilik and Lada must contribute less than ∼3 Jy to the total 2.3 μm flux density of W40. The fact that the contour map presented by Zeilik and Lada appears to be a low resolution version of Figure 1*a* provides further support for the view that emission from compact infrared sources is larger than diffuse 2 μm emission from H II gas or hot dust in W40.

Table 3 gives the photometry plotted in Figure 2 for IRS 1a, 1b, 1c, 2a, and 3a. Entries in Table 3 are in magnitudes. Except where noted in Table 3, 1 σ uncertainties are ± 0.1 mag.

TABLE 2

W40 POSITIONS

Names	α (1950)	δ (1950)
A. Compact Sources		
IRS 1a	18^{h}29^{m}51.7	−2 07′34″
OS 1a	18 29 51.6	−2 07 35
IRS 1b	18 29 52.6	−2 07 42
IRS 1c	18 29 49.9	−2 07 28
OS 1c	18 29 49.7	−2 07 29
IRS 1d	18 29 51.4	−2 07 23
OS 1d	18 29 51.4	−2 07 22
IRS 2a	18 29 47.8	−2 07 41
OS 2a	18 29 47.5	−2 07 40
IRS 2b	18 29 46.5	−2 07 45
OS 2b	18 29 46.1	−2 07 43
OS 2c	18 29 49.0	−2 07 21
IRS 3a	18 29 47.8	−2 06 21
OS 3a	18 29 47.8	−2 06 22
OS 4a	18 29 50.3	−2 06 42
B. Large-Scale Sources		
H II	18 29 49.0	−2 07 35
CO-Peak 1	18 29 39.7	−2 09 58
CO-Peak 2	18 29 39	−2 04 25
AFGL 2177	18 29 47	−2 07 36

NOTE.—Where appropriate, an infrared source (IRS) is paired with its corresponding optical source (OS). Infrared source positions were measured at 2.3, 3.6, or 10 μm and with 5″ apertures. Optical source positions were measured on a print of the Palomar Observatory Sky Survey E series, a portion of which is reproduced in Fig. 1*f*. Positions (1b) referring to large-scale components of the W40 complex were measured with ∼3′ apertures. Published 1 σ uncertainties are ∼20″ for the position of peak H II emission (Goss and Shaver 1970) and ∼2″ for AFGL 2177 (Price and Walker 1976). Positions of peak ^{12}CO ($J = 1 \rightarrow 0$) emission were taken from Zeilik and Lada 1978.

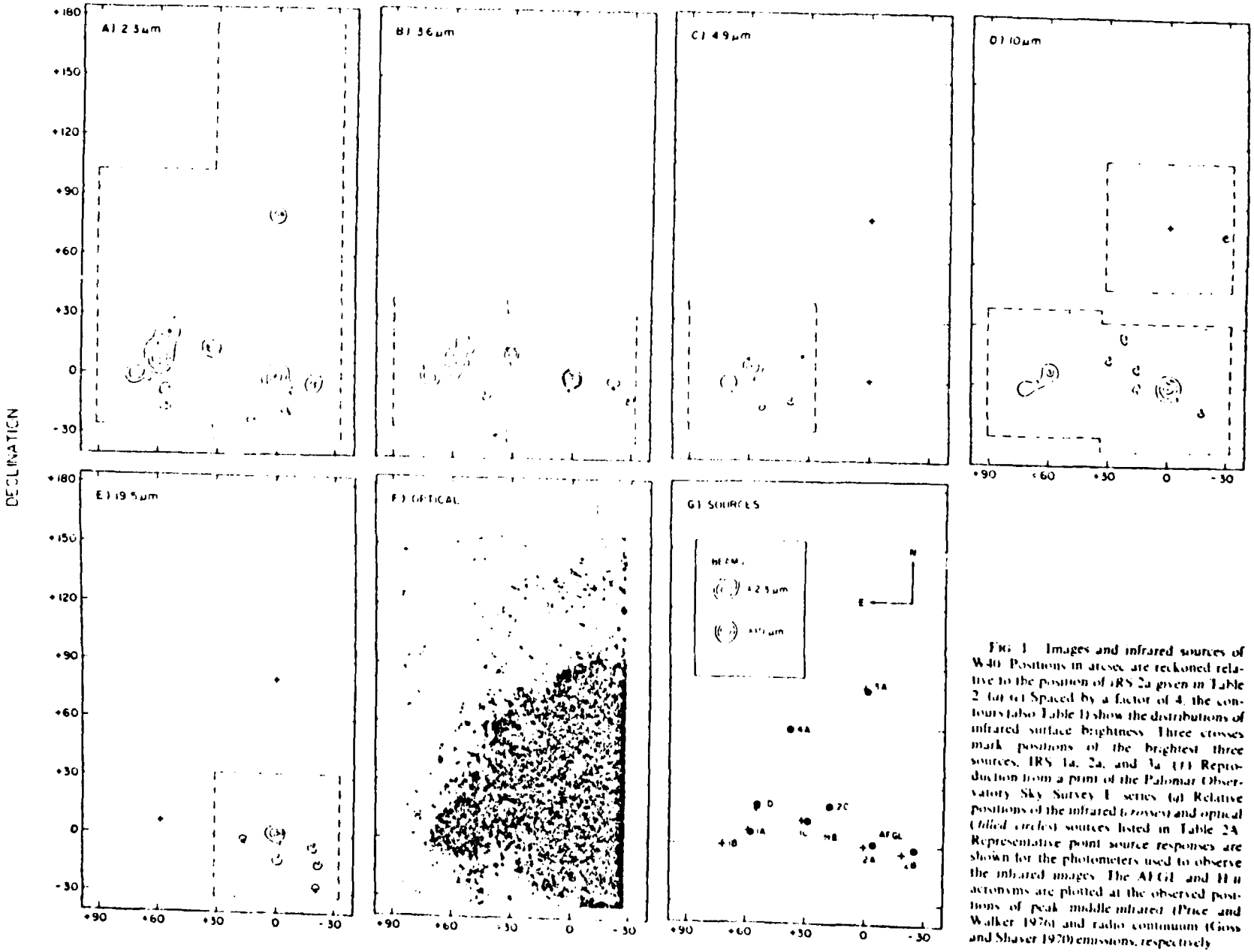

FIG. 1.—Images and infrared sources of W40. Positions in arcsec are reckoned relative to the position of IRS 2a given in Table 2. (a) to (e) Spaced by a factor of 4, the contours (also Table 1) show the distributions of infrared surface brightness. Three crosses mark positions of the brightest three sources, IRS 1a, 2a, and 3a. (f) Reproduction from a print of the Palomar Observatory Sky Survey I series. (g) Relative positions of the infrared (*crosses*) and optical (*filled circles*) sources listed in Table 2A. Representative point source responses are shown for the photometers used to observe the infrared images. The AFGL and H II acronyms are plotted at the observed positions of peak middle infrared (Price and Walker 1976) and radio continuum (Gioss and Shaver 1970) emissions, respectively.

TABLE 3

W40 PHOTOMETRY

Source	IRS 1a	IRS 1b	IRS 1c	IRS 2a	IRS 3a
$U-B$	0.6	...	...	1.1	0.9
$B-V$	2.2	...	...	2.7	2.4
V	15.0	...	...	16.1	15.6
$J-H$	1.3	...	...	1.6	0.9
$H-K$	1.0	...	...	0.9	0.5
$K-L$	1.3	2.0	1.1	1.7 ± 0.2	0.4
L	4.3	5.7	7.1	4.6	7.3
$L-M$	0.6	0.9	0.7	1.0	0.7
$L-[8.7\ \mu m]$	1.7	2.4	2.2	3.8	2.7 ± 0.2
$L-N$	1.8	2.7	2.4	4.5	3.2
$L-[11.4\ \mu m]$	2.2	3.1	2.6	5.0	3.4
$L-[12.6\ \mu m]$	2.3	2.9 ± 0.2	...	5.3	4.0 ± 0.2
$L-[19.5\ \mu m]$	3.2	4.7 ± 0.4	...	6.7	5.3 ± 0.4
$L-[23\ \mu m]$	...	...	...	7.5 ± 0.2	...

The shapes of the infrared energy distributions given in Figure 2 demonstrate that the three sources seen in the 10 μm images (IRS 1a, 1b, and 2a) have circumstellar emission. Flux densities of IRS 2a increase from 10 to 23 μm in a fashion expected of warm circumstellar dust. Infrared sources 1a and 1b show broad, roughly constant distributions of infrared flux density possibly from circumstellar material having a wide temperature range. Notice that photospheric radiation from a main-sequence star would have a monotonically decreasing flux density as the infrared wavelength increases.

Figure 2 presents evidence for circumstellar emission from two additional sources (IRS 1c, 3a) too faint to be imaged at 10 μm. At $\lambda \geq 10$ μm, IRS 3a resembles IRS 2a, whereas IRS 1c has a broad infrared energy distribution much like that shown for IRS 1a. The small amount of information given in Figure 2b for IRS 1d and 2b was inferred from the 2.3 and 3.6 μm images of Figure 1.

From 3.6 to 12.6 μm, the energy distribution shapes (Fig. 2b) of IRS 1b and 1c resemble the approximately flat energy distribution of their nearest bright neighbor, IRS 1a. A noteworthy difference among the three energy distributions is the abrupt decrease occurring between 3.6 and 2.3 μm for IRS 1b, the only source of the three that has no visible companion on the POSS E print. Possible explanations of these two differences in IRS 1b are that it has a larger extinction or an intrinsically fainter star.

Zeilik and Lada (1978) give some energy distribution information for their sources, IRS 1, 2, and 3. Their data, observed with three different aperture sizes and a reference aperture spacing of 100", can be compared with our detailed energy distributions of IRS 1a, 2a, and 3a, each observed with a 5" aperture and a 60" reference aperture spacing. Zeilik and Lada observed IRS 1 with an 18" aperture. At K and L, their photometry of IRS 1 and our photometry of IRS 1a agree reasonably well. Beyond 3.6 μm, the photometry of IRS 1 and IRS 1a differ: the energy distribution of IRS 1 increases strongly from 5 to 20 μm in a fashion expected of warm dust, whereas IRS 1a shows a broad and nearly flat energy distribution. The energy distributions given by Zeilik and Lada for IRS 2 and 3 cover the small wavelength ranges of 1.65–5.0 and 1.25–5.0 μm, respectively. Observed through a 16" aperture, their photometry of IRS 2 agrees reasonably well with our photometry of IRS 2a. In contrast, their photometry of IRS 3, observed through a large 46" aperture, differs from our photometry of IRS 3a: IRS 3 is fainter at J and H but brighter at the larger K and L wavelengths. In summary, the photometric observations reported by Zeilik and Lada are brighter than or equal to our values at K and longer wavelengths; at the shorter J and H wavelengths, their data are equal to or fainter than ours.

The way in which the WIRO and Zeilik and Lada energy distributions depend on aperture size and reference aperture spacing suggests that W40 has extended distributions of infrared emission. Some good evidence for extended emission from interstellar dust is the large ratio of IRS 1 IRS 1a flux densities

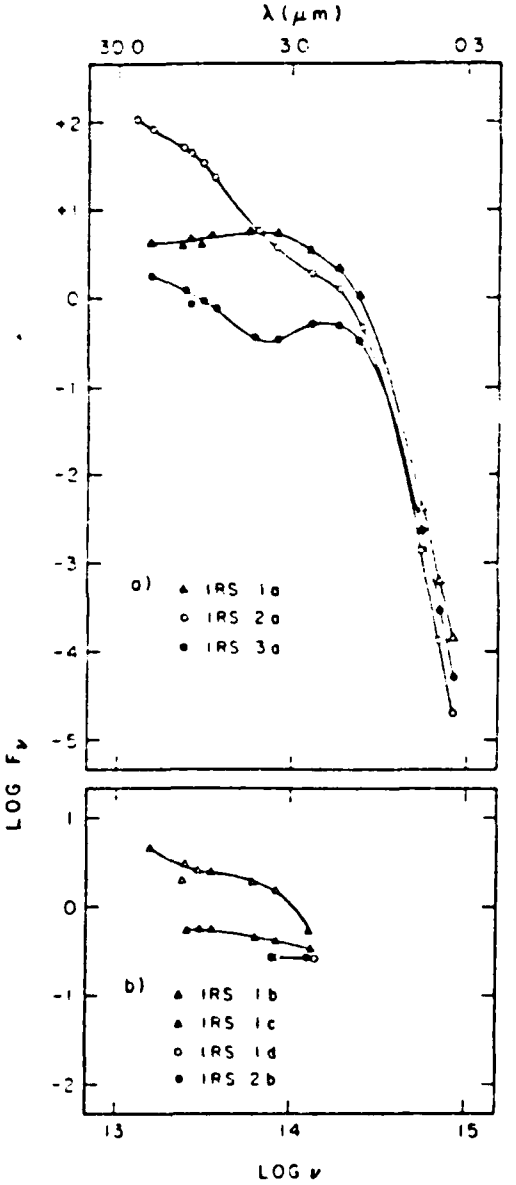

FIG. 2.—Energy distributions of the seven infrared sources observed in W40. Logarithm of flux density (F_ν, in Jy) is plotted against logarithm of radiation frequency. Solid lines show smooth trends in the data plotted for each source. See Table 3 for the broad-band photometry plotted for IRS 1a, 1b, 1c, 2a, and 3a. Flux densities of IRS 1d and 2b were inferred from the infrared images shown in Figs. 1a and 1b. (*a*) Optical through infrared energy distributions of IRS 1a, 2a, and 3a. (*b*) Infrared energy distributions of IRS 1b, 1c, 1d, and 2b. The upper limit plotted at 3.6 μm for IRS 2b is 3 σ.

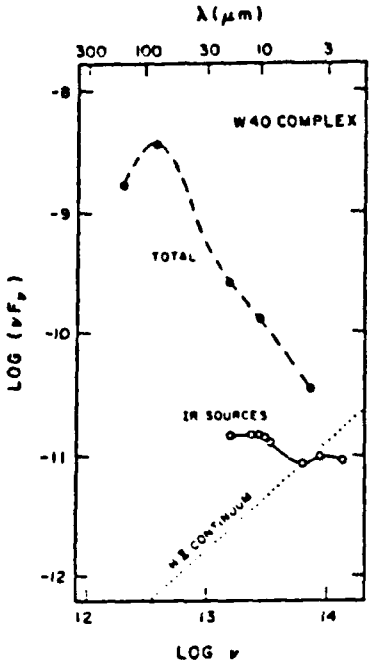

FIG. 3.—Infrared energy distributions of the W40 complex. Logarithm of the product of frequency times flux density (νF_ν, in W m^{-2}) is plotted against logarithm of the frequency. Extending from 2.3 to 19.5 μm, the solid line shows the nearly flat spectral distribution of the sum (open circles) of the flux densities measured for the five brightest infrared sources and given individually in Table 3. Connected by the dashed line, filled circles show the 4, 11, and 20 μm measurements made by Price and Walker (1976) with a 3.5 × 10.5 aperture and the 55 and 155 μm measurements made by Olthof (1974) with a 30′ aperture. The monotonically increasing dotted line is an unextinguished extrapolation of the 1.4–5.0 GHz H II emissions measured by Altenhoff *et al.* (1970) with an 11′ aperture.

amounting to a factor of ~10 in the 10–20 μm interval. In addition, photometric errors may contribute to the large difference between observations of IRS 1 and 1a. The differences observed between IRS 3 and IRS 3a may require extended emissions of two types: emission from hot interstellar dust may explain the differences observed at *K* and *L*, whereas photospheric emission produced by the widely distributed infrared cluster of W40 (Smith 1984) may explain the differences observed at the shorter *J* and *H* wavelengths.

The presentation of Figure 3 reveals some additional information concerning the origin of infrared emissions observed in W40. Total flux densities were inferred from the large beam measurements of Price and Walker (1976) and Olthof (1974) made at middle-infrared and far-infrared wavelengths, respectively. The contribution of compact infrared sources to each total flux density is approximated by the sum of the flux densities measured for IRS 1a, 1b, 1c, 2a, and 3a (Table 3); using the low-resolution observations of IRS 1, 2, and 3 made by Zeilik and Lada (1978) would make no qualitative difference in our discussion. For observed wavelengths of the 10–20 μm interval, the combined emission of the five infrared sources accounts for < 10% of the total emission. This small contribution of the infrared sources and also the shape of the W40 energy distribution suggest that diffuse clouds of dust having a wide temperature range produce almost all the middle-infrared and far-infrared emissions observed for W40. About 96% of the total W40 emission is produced beyond 20 μm, suggesting that the cool component of the diffuse dust is the predominant source of reradiation in W40. Much of the 4% remainder emitted short of 20 μm appears to be produced by a warm component of the diffuse dust possibly closely associated with the H II plasma. Near 4 μm, the total emission must be produced by a complex combination of sources including the infrared sources and the H II gas, each of which contributes ~25% of the total amount.

Before the levels of excitation can be estimated for the diffuse clouds of dust and H II gas in W40, their distance must be specified. The distance adopted for our work is 700 pc (Goss and Shaver 1970). This value was inferred from recombination line observations of the W40 H II region and the kinematic model of the Galaxy. Another datum that tends to confirm this relatively small distance of W40 is its galactic latitude of 3.5. This latitude requires that W40 be no more distant than ~800 pc if it is to reside within the ~100 pc thick plane normally populated by the Galaxy's H II regions.

The level of dust cloud excitation may be inferred from the infrared observations given for the W40 complex in Figure 3. Summing the fluxes implied by the dashed curve gives 5×10^{-9} W m^{-2} for the 4–200 μm flux of the W40 complex. That flux, or its equivalent luminosity of $7.5 \times 10^4\ L_\odot$, could originate from dust heated by a single O9 V star. This same O9 V level of excitation can be calculated for the H II gas from radio observations. For the H II region of W40, Altenhoff *et al.* (1969) give 35 Jy for the radio continuum emission and Pankonin, Thomassohn, and Barsuhn (1977) give $He^+/H^+ = 0.09$ for the 166α ratio of recombination line fluxes. Both the Lyman-continuum luminosity of $\sim 1.5 \times 10^{49}$ photon s^{-1} inferred from the continuum emission and the approximate excitation temperature implied by the recombination ratio could be produced by a single O9 V star.

IV. DISCUSSION

a) Energy Distributions of the Compact Sources

The evaluation of accurate monochromatic extinctions is a crucial part of any attempt to decompose an observed energy distribution into circumstellar and photospheric components. Table 4 gives results of the sequence of steps leading to the monochromatic extinctions of W40-IRS 3a. First, we found that the IRS 3a photometry of the 0.55–4.9 μm interval could be explained by the photospheric emission of a B1 V star lying at the W40 distance of 700 pc and obscured by a standard type of interstellar extinction (Savage and Mathis 1979). As a result, the $E[V-\lambda]$ excess colors were computed as the observed colors (the $V-[\lambda]$) minus the intrinsic colors of a B1 V star

TABLE 4

MONOCHROMATIC EXTINCTIONS OF W40 IRS 3a

λ (μm)	$V-[\lambda]$ (mag)	$E[V-\lambda]$ (mag)	A_λ (mag)	A_λ/A_V
0.36	−3.3	−4.5	...	14.5
0.44	−2.4	−2.7	...	12.7
0.55	...	...	...	10.0
1.25	6.7	7.3	10.1	2.8
1.65	7.6	8.3	10.2	1.9
2.3	8.0	8.8	9.9	1.2
3.6	8.3	9.2	9.8	0.6
4.9	9.0	9.9	10.1	0.2
10.0	11.1	12.1	...	0.0
Mean				1.0

(Johnson 1966). Using the five excess colors of the 0.55–4.9 μm interval and standard interstellar values of $A_\lambda/E(V-\lambda)$, we computed 10.0 mag for the mean visual extinction of IRS 3a. The last step of the extinction analysis was to use the derived 10.0 mag of visual extinction to compute each of the values of monochromatic extinction (A_λ). For $\lambda \geq 0.55$ μm, each value of A_λ was computed as the product of the 10.0 mag and the appropriate standard value of A_λ/A_V. For the shorter B and U wavelengths, the monochromatic extinctions were computed directly from the excess colors as $10.0 + E(B-V)$ and $10.0 + E(U-V)$. Values of $A_V/E(B-V)$ and $A_V/E(U-V)$ implied by this analysis are 3.8 and 2.2, respectively. Differing little from the standard values of 3.1 and 1.9, those extinction ratios emphasize the predominantly standard nature of the monochromatic extinctions affecting the observed energy distribution of IRS 3a.

Figure 4 shows the energy distribution of W40-IRS 3a decomposed into photospheric and circumstellar components. The photospheric energy distribution is normalized to the V flux density of IRS 3a and has the shape determined by the intrinsic colors of a B1 V star modified by the monochromatic extinctions of Table 4. The circumstellar energy distribution of IRS 3a, derived by subtracting the photospheric flux densities from the observed values, is indicative of warm circumstellar dust at ~ 270 K. The circumstellar luminosity of the 5–20 μm interval is $\sim 4\ L_\odot$ or $\sim 0.01\%$ of the total luminosity of a B1 V star.

Unlike the colors of IRS 3a, the colors of IRS 1a and 2a do not show convincing evidence for predominantly photospheric emission extending from optical to near-infrared wavelengths. Therefore, we must seek an alternative to the method of inferring a mean value of visual extinction from the observed optical-infrared colors. A reasonable alternative is to use the IRS 3a ratios of $A_V/E(B-V)$ and $A_V/E(U-V)$ together with values of the excess colors, $E(B-V)$ and $E(U-V)$. For each star, the excess colors were computed from the observed colors

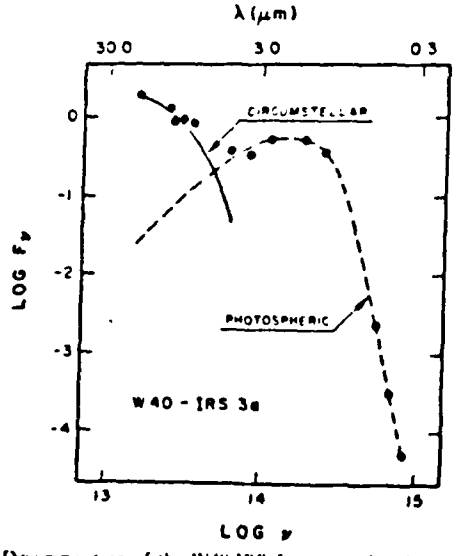

FIG. 4.—Decomposition of the W40-IRS 3a energy distribution into circumstellar and photospheric components. Observed data are plotted as *filled* circles. Data observed for the 0.55–4.9 μm interval are fitted to the photospheric emission of a B1 V photosphere (*dashed line*) obscured by interstellar dust producing $A_V = 10$ mag. Shown connected by the solid line, the circumstellar flux densities are the observed minus the photospheric flux densities.

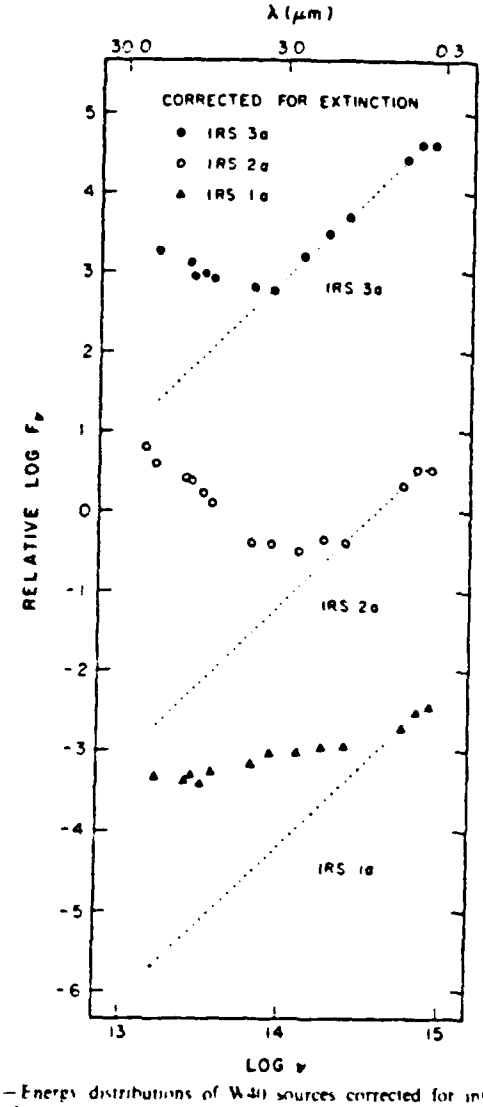

FIG. 5.—Energy distributions of W40 sources corrected for interstellar extinction. Each dotted line shows the shape of a B1 V energy distribution normalized to the corrected V flux density. A displays constant (C) added to the logarithm of flux density (F_ν in Jy) is plotted against logarithm of radiation frequency. Values of C are +3, −4.3, and −4 for IRS 3a, 2a, and 1a, respectively.

(Table 3) and B1 V as a noncritical approximation to the spectral type. Values of mean visual extinction inferred by this alternative method are 9.2 and 11.3 mag for IRS 1a and 2a, respectively. Monochromatic extinctions are inferred from each of these values of visual extinction in the same way described above for IRS 3a.

Figure 5 shows the energy distributions of IRS 1a, 2a, and also 3a corrected for the interstellar extinctions computed above. Also plotted in Figure 5 are the energy distributions of a B1 V photosphere normalized to the corrected visual flux density of each star. Although circumstellar emission becomes important for IRS 3a only at wavelengths longer than 4.9 μm, it dominates the energy distributions of IRS 1a and 2a at much shorter wavelengths.

It proves informative to compare the W40 sources with other objects which have been studied in some detail. Figure 6*a*

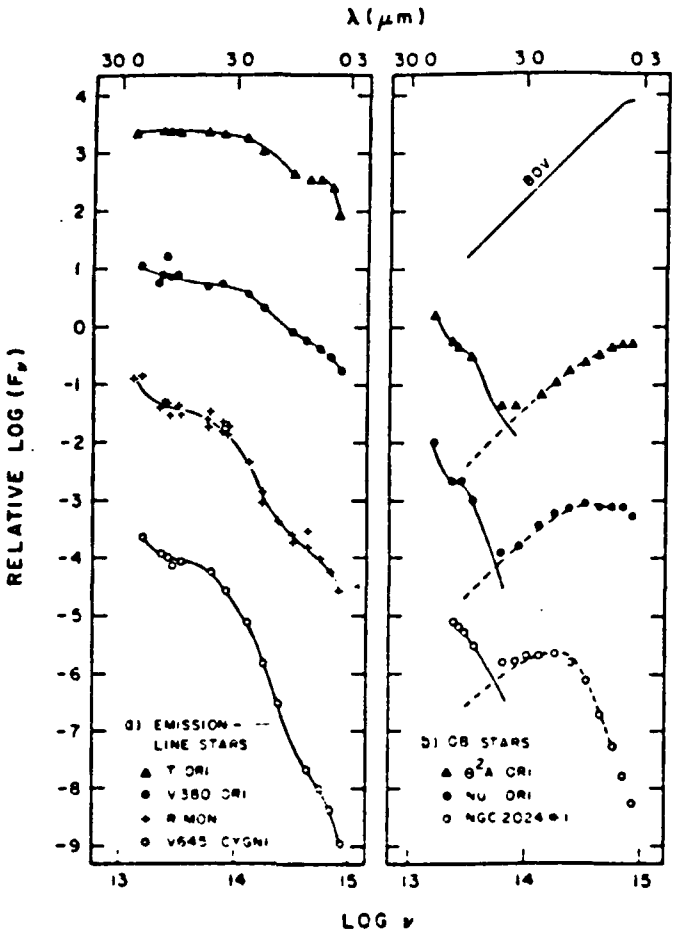

FIG. 6.—Energy distributions of comparison stars used to study the observed W40 sources. For each star of the two panels, a display constant (C) added to the logarithm of flux density (F_ν in Jy) is plotted versus the logarithm of observed radiation frequency for a sequence of hot, emission-line stars ordered according to their 10–0.55 μm ratio of flux densities. Similar to W40-IRS 1a, 1b, and 1c, $F_\nu \approx$ constant for substantial portions of the infrared energy distributions. Solid curves show merely trends in the flux densities. Values of C are +3, 0, −3, and −6 for T Ori (B8–A2pe), V380 Ori (B5–A2e), R Mon (e + shell), and V645 Cygni (A5e), respectively. References for the plotted flux densities are Walker (1969), Penston (1973), and Smith (1978) for T Ori; Lee (1970), Low *et al.* (1970), Cohen (1973), and Allen (1973) for V380 Ori and R Mon; and Humphreys, Merrill, and Black (1980) for V645 Cygni. References for the emission-line spectra are Johnson (1965) for T Ori, Herbig (1959, 1962) for V380 Ori and R Mon, Humphreys *et al.* for V645 Cygni. (*b*) Extinction sequence of comparison OB stars related to W40-IRS 3a. Symbols show the observed flux densities. Photospheric flux densities (*dashed lines*) were computed from intrinsic stellar colors modified by interstellar extinction. Connected by a solid line for each star, circumstellar flux densities are the observed minus the photospheric flux densities. Values of $(A_\nu)_0$ are (0.0), (1.1, −2.0), (2.2, −4.0), and (3.3 mag, −6.0) for the intrinsic energy distribution of a B0 V star (top, $V = 0$ mag). θ^2 A Ori (O9.5 Vp), NU Ori (B0.5 Vp), and NGC 2024 No. 1 (bottom, B0.5 Vp), respectively.

shows the energy distributions of four comparison stars, T Ori, V380 Ori, R Mon, and V645 Cygni, each of which is a hot emission-line star associated with nebulosity. Like W40-IRS 1a, 1b, and 1c, the emission-line stars tend to have $F_\nu \approx$ constant for a substantial portion of their 2–20 μm energy distributions. Thus, IRS 1a, 1b, and 1c may be hot emission-line stars. Figure 6*b* shows the energy distributions of three additional comparison stars, θ^2 A Ori, NU Ori, and NGC 2024 No. 1, each of which is a relatively normal OB star with a reradiating circumstellar dust cloud. Like W40-IRS 3a, each of these OB stars has a circumstellar energy distribution that increases strongly from 5 to 20 μm. Thus, the case is strengthened for IRS 3a being a main-sequence OB star surrounded by a cloud of reradiating dust grains. Figure 5 shows that W40-IRS 2a has characteristics of both the emission-line and main-sequence OB stars: for the 1–5 μm interval, the corrected flux densities of IRS 2a are nearly constant, whereas, for wavelengths longer than 5 μm, the energy distribution of IRS 2a increases strongly like those of the main-sequence OB stars.

The summary presented in Table 5 includes descriptions of W40-IRS 3a and the three comparison stars, θ^2 A Ori, NU Ori, and NGC 2024 No. 1. The above analysis of IRS 3a gives the guidelines used to derive monochromatic extinctions for each of the comparison stars. For each of IRS 3a, θ^2 A Ori, NU Ori, and NGC 2024 No. 1, the value of L_c/L_{ir} shows that circumstellar emission (L_c) is a substantial portion of the total infrared emission (L_{ir}). However, relative to the photospheric emission (L_*) estimated for each star, the value of L_c is small. Thus, very little of each star's luminosity is reradiated by circumstellar dust at 5–20 μm.

Because the photospheric components are very difficult to identify for IRS 1a and 2a, the summaries presented in Table 5 for these two stars are relatively uncertain. Nevertheless, these summaries should be useful for purposes of comparison. Each

TABLE 5

PROPERTIES OF SELECTED SOURCES

Source	Sp	A_v (mag)	$\frac{A}{E(B-V)}$	$\frac{A_v}{E(L-V)}$	V_0 (mag)	M_v (mag)	T_c (K)	T_B (K)	L_{IR} ($L_\odot$)	L_c ($L_\odot$)	$\frac{L_c}{L_{IR}}$ (percent)	$\frac{L_c}{L_*}$ (percent)
A. Compact W40 Sources												
IRS 1a	(OB)	9	(3.8)	(2.2)	5.8	−3.5	350	79	90	(80)	(90)	(0.3)
IRS 1b	...	...	...	...	...	...	280	77	30	...	...	...
IRS 1c	...	...	...	...	...	...	...	71	>7	...	...	...
IRS 2a	(OB)	11	(3.8)	(2.2)	4.9	−4.3	250	89	230	(220)	(96)	(0.3)
IRS 3a	(OB)	10	3.8	2.2	5.5	−3.7	270	73	10	4	40	(0.01)
B. Embedded OB Stars												
9 Aql	O9.5V	1.1	4.7	2.8	4.0	−4.0	200	...	100	90	80	0.1
NU Ori	B0.5V	2.2	4.1	2.4	4.6	−3.4	170	...	50	40	80	0.2
NGC 2024 No. 1	B0.5V	7.8	4.6	2.6	4.4	−3.6	...	...	>13	>5	>40	>0.02

NOTE.—The optical and infrared photometric data used in calculating the entries were taken from Table 3 for the sources of W40, from Lee 1968, Iriarte *et al.* 1965, Pension 1973, and Ney, Strecker, and Gehrz 1973 for 9 Aql Ori and NU Ori, and from Johnson 1966 and Grasdalen 1974 for NGC 2024 No. 1. A specific OB spectral type of B1 V was adopted in analyses of the W40 sources, depending on future spectral classification work. Values enclosed within parentheses may be revised. Iriarte *et al.* 1965, Schild and Chaffee 1971, and Johnson and Mendoza 1974 give the spectral types for 9 Aql Ori, NU Ori, and NGC 2024 No. 1, respectively. The text describes how the values of visual extinction (A_v) were computed. Intrinsic visual magnitudes are given by $V_0 = V - A_v$. Distance moduli (DM) used in computing the absolute visual magnitudes ($M_v = V_0 - DM$) and luminosities (L_{IR}, L_*, L_c) are 9.2 and 8.0 mag for the W40 and other sources, respectively. Blackbody color temperatures (T_c) are computed from the 10–20 μm ratio of flux densities. Each blackbody brightness temperature (T_B) refers to the source + 20 arcsec surface brightness averaged over the ~20 arcsec² aperture. Values of L_{IR} are total amounts of infrared luminosity produced in the 2.2–20 μm wavelength interval. Values of L_c are the circumstellar portions of the values of L_{IR}. Photospheric luminosities (L_*) were computed from the values of M_v and bolometric corrections (Code *et al.* 1976) implied by the spectral types.

of the three sources. IRS 1a, 2a, and 3a, consists of a heavily obscured OB star associated with a compact circumstellar source. This interpretation differs in two basic ways from the view developed by Zeilik and Lada (1978) for their low-resolution observations of W40. They described their three brightest sources not as being compact but as resolved, ~30" diameter regions of diffuse emission. Second, they argued that extinction by dust should not affect substantially the W40 energy distributions, whereas our analysis implies substantial values of ~10 mag for the visual extinctions.

b) *Morphology and Energetics*

Basic elements of the W40 morphology (Fig. 7) include (1) the brightest and therefore probably densest portion of the extensive molecular complex observed by Zeilik and Lada (1978), (2) the large, ~5′ diameter H II region (Goss and Shaver 1970; Altenhoff *et al.* 1970) lying in a side-by-side and possibly contiguous relationship with the bright molecular core, and (3) the seven detected infrared sources distributed within a 1′.5 diameter region centered approximately on the position of peak H II emission.

The close association of the infrared sources with the H II region, the absolute visual magnitudes (M_v) summarized in Table 5, and the level of excitation derived for both the dust and H II gas (S III) suggest that some combination of the brightest detected sources (IRS 1a, 2a, 3a) has enough luminosity to ionize the H II gas and heat much of the dust of the W40 complex. IRS 2a appears to be the most luminous star; we suggest that it is the most important single source of excitation.

Estimates of extinction optical depths constrain the possible modes whereby the observed sources heat the dust distributed throughout the W40 complex. To compute extinction optical depths for the dust, we assume that the dust extinctions obey a standard interstellar curve (Savage and Mathis 1979) and that optical reddening is related to the nucleon column density according to the standard interstellar relation given by Bohlin, Savage, and Drake (1978). These two assumptions lead to $A_v \approx 1 \times 10^{-21} N_H$ mag, the desired relation between the ultraviolet extinction (A_v) and the nucleon column density (N_H). Using this relation, we estimate ultraviolet extinctions of $\lesssim 3$ and ~30 mag for the columns of dust associated with the H II and molecular gases, respectively. For the H II region, N_H

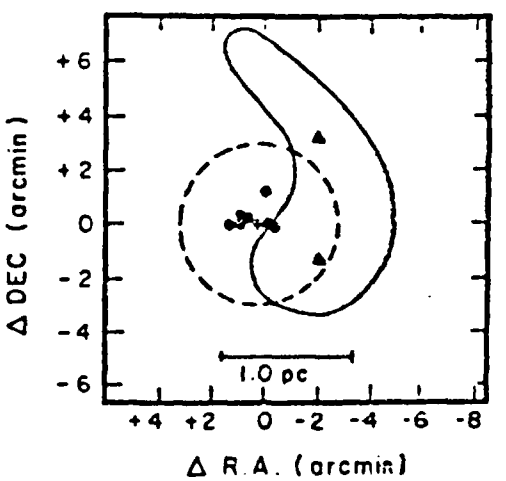

FIG. 7.—Elements of the W40 morphology. Shading shows where emission from the CO molecule has been detected in the 14′ × 14′ region covered by the figure. The solid line encloses the bright molecular core for which the peak brightness temperatures of CO ($J = 1 \rightarrow 0$) emission are in the 15–31 K range. The positions of peak CO emission are plotted as filled triangles. Centered at the cross, plotted ~2.5 northwest of the position of brightest CO emission, the 5′ diameter H II region (dashed line) lies side by side with the molecular core. Filled circles show positions of the seven detected infrared sources all of which lie near the position of peak H II emission. Positions in arc minutes are reckoned relative to the IRS 2a position plotted as (0, 0). At the adopted distance of 700 pc, the scale is 1′ = 0.20 pc.

was equated to the $\sim 1 \times 10^{21}$ cm^{-2} electron column density (Shaver and Goss 1970); A_{vv} is an upper limit because dust that would ordinarily be associated with the $\sim 1 \times 10^{21}$ cm^{-2} column density of nucleons may be modified or expelled by the harsh ultraviolet radiation field of the H II region. For the molecular complex, wherein $N_H = 2N_{H_2}$ applies, we computed a peak value of N_H from $N_{H_2} = 5 \times 10^5 N_{13}$ (Dickman 1978) and $N_{13} \simeq 5 \times 10^{16}$ cm^{-2}, the ^{13}CO column density given by Zeilik and Lada (1978) for the position of Peak 1 (Table 1). Using the relative distribution of $^{12}CO(J = 1 \rightarrow 0)$ emission (Zeilik and Lada 1978) to scale the peak column density gives $N_H \simeq 3 \times 10^{22}$ cm^{-2} for molecules distributed along the lines of sight intercepting the embedded infrared sources.

Now that we have proposed the major sources of excitation and estimated some extinction optical depths for the volume of W40, we can proceed to discuss some general aspects of the dust cloud energetics. A small portion of the total amount of diffuse dust, surrounding the cluster and having $A_{vv} \simeq 1$, could absorb and then reradiate much of the cluster's luminosity. Depending on whether dust is depleted in the H II region and also on the accuracy of the above extinction calculation, much of this dust with $A_{vv} \simeq 1$ may reside within an interface between the H II boundary and molecular cloud. This leaves a large amount of cooler dust, mixed with the molecules and isolated by significant ultraviolet extinction from the energetic sources of the H II region, to be heated by radiation from a complex combination of sources including the obscured exciting stars, additional members of the widely distributed W40 star cluster (Smith 1984), and the warm dust grains near the H II region. Each of the two dust components will contribute to the total reradiation spectrum of the W40 complex, but the small amount of diffuse dust irradiated directly by the exciting stars will contribute most to the far-infrared reradiation.

A small amount of diffuse dust may lie within the circumstellar region of each of the infrared stars. Although this hypothetical component would have a negligible impact on the energetics of W40, we can show that its presence could account for a significant portion of the circumstellar emissions observed for IRS 2a and 3a. We can estimate the size of a cloud of diffuse dust for which $L_* \cdot L_\star < 0.01 L_\star$, a limit to the levels given for the 5–20 μm reradiations of IRS 2a and 3a (Table 5). Along its diameter, the cloud would produce $A_{vv} \simeq 2L_\star$ for the extinction at ultraviolet wavelengths or $< 1\%$ of the ~ 3 mag estimated for the assumed unmodified dust mixed with the plasma. If 5" roughly the observed width of the H II region, approximates the distance to which the 3 mag refers, then the diffuse cloud would be $< 2"$ in diameter. In addition to this compact size, we would expect the circumstellar component of the diffuse dust to have a 10–20 μm color temperature larger than the ~ 200 K *inferred* from the AFGL measurements made with a large beam (Fig. 3). Both expected properties of the diffuse circumstellar emission are consistent with the observations: the images show that IRS 2a is compact at both 10 and 20 μm and the sets of photometry give ~ 250 K for the 10–20 μm color temperatures of IRS 2a and 3a.

The differences in shape observed for the infrared energy distributions of IRS 1a, 2a, and 3a suggest some intrinsic differences among their circumstellar regions. Harvey, Thronson, and Gatley (1979) have discussed how the shape of a circumstellar energy distribution may depend on the density profile of the circumstellar material. One of their models suggests that strongly increasing energy distributions of the type observed at $\lambda \gtrsim 10$ μm for IRS 2a and 3a are produced by circumstellar dust grains having a uniform density. Within the context of this model, our above discussion implies that the uniformly distributed dust surrounding IRS 2a and 3a may be a small portion of the diffuse interstellar medium of W40. A second model considered by Harvey, Thronson, and Gatley (1979) suggests that broad energy distributions of the type observed for the emission-line stars V380 Ori and R Mon (also Fig. 6*a*) are produced by circumstellar condensations of dust. W40-IRS 1a, and possibly IRS 1b and 1c, have broad energy distributions resembling those of the emission-line stars and therefore are candidates for circumstellar condensations.

Being clustered tightly within a small, ~ 0.2 pc diameter region of the W40 complex, the seven W40 sources may have approximately the same epoch of formation. If so, these objects would have roughly the same age yet they have a diverse set of properties. For example, IRS 1a has the $F \simeq$ constant type of circumstellar spectrum, whereas IRS 3a has circumstellar emission that increases strongly beyond ~ 5 μm. Perhaps this diversity of form results from the way that a compact object evolves within its H II region and molecular cloud complex. In the case of W40, the evolution appears to depend in a complex way on the individual evolutions not only of the embedded star and any circumstellar condensation it may have, but also the star's diffuse environment.

V. SUMMARY

We have presented observations revealing a cluster of seven compact infrared sources in W40, all but one of which can be associated with optically identified stars. Being heavily obscured and centered on the H II region, the three brightest sources (IRS 1a, 2a, 3a) are reasonable candidates for producing the level of excitation observed for both the dust and the H II plasma. The circumstellar regions observed for the brightest five sources (IRS 1a, 1b, 1c, 2a, 3a) have little impact on the overall energetics of the W40 dust. Instead, the most important mode of excitation appears to involve the diffuse clouds of dust. The infrared energy distributions exhibit a wide range of shapes, suggesting intrinsic differences among the distributions of circumstellar material.

We thank H. Chisolm and R. Shaw for their work with the detection systems and operations of the telescope. J. Gasaway and M. Lee typed the manuscript. Infrared Astronomy at the Wyoming Infrared Observatory is supported by the NSF, the US Air Force, and the State of Wyoming.

REFERENCES

Allen, D. A. 1973, *M.N.R.A.S.*, 161, 145.
Altenhoff, W. J., Downes, D., Goad, L., Maxwell, A., and Rinehart, R. 1970, *Astr. Ap. Suppl.*, 1, 319.
Bohlin, R. C., Savage, B. D., and Drake, J. F. 1978, *Ap. J.*, 224, 132.
Code, A. D., Davis, J., Bless, R. C., and Hanbury Brown, R. 1976, *Ap. J.*, 203, 417.
Cohen, M. 1973, *M.N.R.A.S.*, 161, 105.
Dickman, R. 1978, *Ap. J. Suppl.*, 37, 407.
Gehrz, R. D., Grasdalen, G. L., Castelaz, M., Gullixson, C., Mozurkewich, D., and Hackwell, J. A. 1982, *Ap. J.*, 254, 550 (Paper III).
Gehrz, R. D., Hackwell, J. A., and Jones, T. W. 1974, *Ap. J.*, 191, 675.
Goss, W. M., and Shaver, P. A. 1970, *Australian J. Phys. Ap. Suppl.*, No. 14, p. 1.

Hackwell, J. A., Grasdalen, G. L., and Gehrz, R. D. 1982, *Ap. J.*, 252, 250 (Paper I).
Harvey, P. M., Thronson, H. A., and Gatley, I. 1979, *Ap. J.*, 231, 45.
Hoag, G. H. 1959, *Ap. J. Suppl.*, 4, 337.
Kron, G. E. 1962, *Ann. Astr. Ap.*, 2, 1.
Humphreys, R. M., Merrill, K. M., and Black, J. H. 1980, *Ap. J. (Letters)*, 237, L17.
Iriarte, B., Johnson, H. L., Mitchell, R. I., and Wisniewski, W. K. 1965, *Sky and Tel.*, 30, 21.
Johnson, H. L. 1966, *Ann. Rev. Astr. Ap.*, 4, 193.
Johnson, H. L., and Mendoza, E. E. 1964, *Bol. Obs. Tonantzintla y Tacubaya*, 3, 331.
Johnson, H. L., Mitchell, R. I., Iriarte, B., and Wisniewski, W. Z. 1966, *Comm. Lunar Planet. Lab.*, No. 63.
Johnson, H. M. 1965, *Ap. J.*, 142, 964.
Lee, T. A. 1968, *Ap. J.*, 152, 913.
Lee, T. J. 1970, *Pub. A.S.P.*, 82, 765.
Low, F. J., Johnson, H. L., Kleinmann, D. E., Latham, A. S., and Geisel, S. L. 1970, *Ap. J.*, 160, 531.
Ney, E. P., Strecker, D. W., and Gehrz, R. D. 1973, *Ap. J.*, 180, 809.
Olthof, H. 1974, *Astr. Ap.*, 33, 471.
Pankonin, V., Thomasson, P., and Barsuhn, J. 1977, *Astr. Ap.*, 54, 335.
Penston, M. V. 1973, *Ap. J.*, 183, 505.
Price, S. D., and Walker, S. G. 1976, *AFGL Four Color Infrared Sky Survey* (Environmental Research Papers No. 576).
Savage, B. D., and Mathis, J. S. 1979, *Ann. Rev. Astr. Ap.*, 17, 73.
Schild, R. E., and Chaffee, F. 1971, *Ap. J.*, 169, 529.
Smith, J. 1976, Ph.D. thesis, University of Wyoming.
——. 1984, private communication.
Walker, M. F. 1969, *Ap. J.*, 155, 447.
Zenik, M., and Lada, C. J. 1978, *Ap. J.*, 222, 896.

A. BENTLEY, M. CASTILLAZ, R. D. GEHRZ, G. L. GRASDALEN, J. A. HACKWELL, and J. SMITH: Department of Physics and Astronomy, The University of Wyoming, University Station, Box 3905, Laramie, WY 82071

THE ASTROPHYSICAL JOURNAL, 292:628–639, 1985 May 15
© The American Astronomical Society. All rights reserved. Printed in U.S.A.

RADIO AND INFRARED OBSERVATIONS OF OH IR STARS AT THE TANGENTIAL POINT AND NEAR THE GALACTIC CENTER

B. BAUD,[1,2] ANNEILA I. SARGENT,[3] M. W. WERNER,[4] AND A. F. BENTLEY[5]
Received 1984 October 10; accepted 1984 November 30

ABSTRACT

We have determined accurate radio positions and subsequently made simultaneous infrared and OH radio measurements of a sample of OH IR stars near the tangential point and in the galactic center. Intrinsic physical parameters of the stars and their dust shells, as well as the maser luminosities, have been determined. They are consistent with the stars being at the top of the asymptotic giant branch; the dense circumstellar shells suggest that they are evolving rapidly through a phase of high mass loss.

Our sample comprises stars of widely different masses and luminosities; it is shown that the OH luminosity is strongly dependent on the degree of reddening of the circumstellar shell, i.e., on the stellar mass-loss rate. In addition, a quantitative relation between the OH luminosity and the optical depth in the 10 μm silicate feature has been determined for the sample. This predicts the observed time variations in the strength of the silicate feature with time-variable stellar luminosity. While the stars in the galactic center sample are systematically less luminous than those at the tangential point, the derived relations apply equally to each group.

Subject headings: infrared: sources — masers — stars: circumstellar shells — stars: late-type

I. INTRODUCTION

Combined infrared and OH observations are essential to understanding the nature of OH IR stars, the properties of their circumstellar envelopes, and the OH maser pump mechanism (cf. Werner *et al.* 1980; Herman 1983). These cool, variable stars, typical of the Asymptotic Giant Branch (AGB) in the H-R diagram, have generally been found through OH radio surveys (e.g., Johansson *et al.* 1977; Bowers 1978; Baud *et al.* 1979*a*, *b*), and many are strong infrared sources with thick circumstellar dust shells. Since their OH maser emission can be detected at large distances from the Sun, OH IR stars can be used to study the population distribution, kinematics, and evolution of stars on a galactic scale (cf. Baud *et al.* 1981, hereinafter BHMW). Moreover, these objects constitute a unique tool for examining stellar evolution at the tip of the AGB, a region of the H-R diagram which is poorly understood theoretically and where circumstellar obscuration often precludes optical observations. From infrared observations of these objects, the luminosities of the underlying stars and the masses of the circumstellar envelopes may be derived, while the double-peaked OH emission-line profiles yield both the stellar radial velocity v and the circumstellar shell expansion velocity v_e; the latter quantity is statistically related to the main-sequence mass (BHMW). Comparison of the visible, low OH luminosity Mira variables with the optically obscured, but strong OH emitting, OH IR stars indicates that OH luminosity is related to the stellar mass-loss rate, and it has been suggested (Baud and Habing 1983, hereinafter BH; Jones *et al.* 1983) that such OH IR stars represent the end point of the Mira evolution on the AGB; their large mass-loss rates imply that some may be evolving toward a planetary nebula stage.

In this paper we present unambiguous infrared identifications of a sample of OH IR stars in the galactic disk and in the vicinity of the galactic center. Simultaneous OH and broad-band infrared photometric measurements allow us to derive quantitative relations between the infrared and OH fluxes and the properties of the circumstellar shells, providing observational evidence that these stars represent an evolutionary sequence of increasing mass-loss rate. Using these relations, the observed time variations of the silicate absorption feature with changing bolometric luminosity in OH IR stars can be explained. In addition, it appears that the ratio of the OH flux to the number of pump photons is not constant (e.g., Elitzur, Goldreich, and Scoville 1976) but is also a function of the mass-loss rate.

II. OBSERVATIONS

a) *The Sample*

A recurrent problem in determining the physical properties of OH IR objects is the uncertainty and ambiguity in their distances, usually derived kinematically from the observed radial velocities. Most OH IR stars have been discovered in flux-limited radio surveys, so that the near-kinematic distance is a plausible choice (cf. Jones, Hyland, and Gatley 1983), but, since the velocity dispersions are typically 10–30 km s^{-1} (BHMW), the distance uncertainties are large. For example, the near-kinematic distance of OH 26.5 + 0.6 is 1.8 kpc. A more reliable value of 1 kpc, resulting in a significantly lower estimate for the luminosity, has been derived using the observed angular size and the light travel time through the shell (Herman 1983).

The present study includes stars in the galactic plane whose high radial velocities indicate that they are at the tangential point—the position along the line of sight closest to the galactic center—and stars near the galactic center itself. For both groups the distance uncertainties are relatively small. The tangential sample was selected from the homogeneous list of BHMW, which is based on systematic OH surveys of the northern hemisphere (Johannsson *et al.* 1977; Bowers 1978; Baud *et al.* 1979*a*). It consists of (1) all stars with radial velo-

[1] Dept. of Space Research, Groningen, The Netherlands.
[2] Radio Astronomy Lab., University of California, Berkeley.
[3] Owens Valley Radio Observatory, California Institute of Technology, Pasadena.
[4] NASA Ames Research Center, Moffett Field, California.
[5] Dept. of Natural Sciences, Eastern Montana College, Billings.

cities v larger than the maximum velocity v_{max} allowed by circular rotation (cf. Burton and Gordon 1978), and (2) stars with $v > (v_{max} - 10)$ km s^{-1} in cases where $v_e > 15$ km s^{-1}. Stars in the first group are assumed to be at the tangential point; excess velocities presumably reflect random motions. Although some distance ambiguity exists for the second group, the velocity dispersion of these stars is small (~ 10 km s^{-1}; BHMW), and they are probably within 25% of the tangential point.

The galactic center sample was chosen (1) from stars within a degree (170 pc) of the galactic center, with $|v| > 100$ km s^{-1} (Habing *et al.* 1983) and (2) for $l > 1$, from a survey along the galactic plane (Olnon *et al.* 1981; Baud *et al.* 1979*b*). The first group are members of the galactic bulge population (e.g., Olnon *et al.* 1981), where the density of OH IR stars is strongly enhanced. The latter are probably foreground objects and members of the galactic disk population (see appendix A).

The distribution of v_e in both samples is very similar to that for all OH IR stars in the Galaxy (e.g., BHMW), as is the distribution in galactic latitude and longitude. However, since their average distance is large, these stars represent the high-luminosity tail of the OH luminosity distribution: L_{OH} ranges from 1 Jy kpc^2 for the nearby OH-emitting Miras to 1000 Jy kpc^2 for the brightest and most distant OH IR stars (cf. Nguyen-Q-Rieu *et al.* 1979; BH), but for the samples here it is typically larger than 100 Jy kpc^2. Nevertheless, the number of stars in both samples increases steeply with decreasing OH luminosity (see Tables 1 and 2), which is consistent with the OH luminosity distribution found for all OH IR stars (cf. BHMW). Most conclusions drawn from the present sample may therefore be extended to the majority of OH IR stars.

b) Accurate Radio Positions and OH *Fluxes*

Since the OH objects in our sample lie within a degree of the galactic plane, and since single-dish OH measurements lead to positional uncertainties of $\pm 15''$ to $\pm 5'$, confusion with K and M giants along the line of sight can be a serious problem in identifying their near-infrared counterparts (cf. Jones *et al.* 1981, 1982). Interferometric observations of the 1612 MHz OH maser emission were therefore carried out to determine more accurate ($\pm 1''$) radio positions. The need for such positional accuracy is emphasized by the fact that two stars common to this sample and to that of Jones, Hyland, and Gatley (1983) appear to have been misidentified by these authors (see below).

1612 MHz OH observations of the tangential sample were made on two consecutive days in 1980 July with the Very Large Array (VLA) spectral line system of the National Radio Astronomy Observatory.[6] Observations were made with nine telescopes in a hybrid configuration and with baselines ranging from 0.3 to 3.4 km; the synthesized beam was typically $12'' \times 7''.5$. The instantaneous bandwidth of 780 kHz was divided among 128 autocorrelation channels, each 6.1 kHz wide (1.1 km s^{-1}). The instrumental phase and bandpass were calibrated using the unresolved continuum source 1741 − 038 (1.43 Jy based on 13.83 Jy for 3C 286 at 1612 MHz) and 3C 286 respectively.

Positions were determined from high-resolution maps of the high- and low-velocity components of the line profiles. In all cases, emission from the two components appeared unresolved and coincident within the uncertainties of the measurements. The results are listed in Table 1 in order of increasing galactic longitude: column (1) contains the source name and columns (2), (3), (4), and (5) the positions and 3 σ uncertainties in R.A. and Decl. respectively. Although stars from both this and the galactic-center sample are in some cases displaced by 0.1 or more from the single-dish positions, the old source names have

[6] NRAO is operated by Associated Universities, Inc., under contract to the National Science Foundation.

TABLE 1

OH IR Stars at the Tangential Point: Accurate Radio Positions, Velocities, and Peak OH Flux Densities

Name (1)	R.A. (1950) (2)	3 σ (3)	Decl. (1950) (4)	3 σ (5)	LV (km s^{-1}) (6)	HV (km s^{-1}) (7)	S_{LV}* (Jy) (8)	S_{HV}* (Jy) (9)	1 σ (Jy) (10)
OH 10.9+1.5	18°00'42".55	±1.1	−18 41 18.4	±1.2	120.0	144.5	2.61	1.05	0.13
OH 17.2−1.1	18 23 19.55	±0.5	−14 30 08.0	±0.5	158.4	183.3	1.85	3.53	0.13
OH 18.2+0.5	18 19 07.21	±0.3	−12 56 50.2	±0.9	113.9	137.7	1.42	1.96	0.12
OH 18.5+1.4	18 16 47.37	±0.3	−12 09 27.8	±0.9	165.7	187.0	8.45	5.50	0.20
OH 20.7+0.1	18 25 44.32	±0.3	−10 52 51.1	±0.9	117.9	154.6	10.8	6.1	0.6
OH 21.5+0.5	18 25 45.49	±0.6	−10 00 12.4	±0.8	97.8	134.0	25.1	34.1	0.6
OH 24.7−0.1	18 34 03.61	±0.5	−07 20 52.3	±1.1	109.8	142.8	4.8	<1.5	0.5
OH 25.1−0.3	18 35 33.36	±0.6	−07 12 34.9	±1.4	130.0	154.8	7.44	6.60	0.25
OH 27.0−0.4	18 39 21.93	±0.6	−05 24 02.8	±1.1	87.3	116.4	3.71	8.02	0.24
OH 27.2+0.2	18 37 36.72	±0.8	−05 05 28.4	±0.8	72.6	111.4	2.1	2.2	0.3
OH 27.5−0.9	18 42 01.90	±0.6	−05 12 25.5	±0.6	93.0	120.0	7.03	6.11	0.25
OH 27.8−1.5	18 44 57.97	±0.8	−05 14 27.3	±0.9	70.1	100.5	2.27	2.79	0.16
OH 28.5−0.0	18 40 47.45	±0.6	−03 58 57.6	±0.8	93.9	120.6	11.85	11.41	0.24
OH 29.4−0.8	18 45 12.24	±0.4	−03 32 53.2	±1.4	113.6	137.3	10.35	5.81	0.27
OH 30.1−0.7	18 46 04.91	±0.3	−02 53 54.1	±0.8	78.4	119.0	57.2	59.6	0.4
OH 31.0−0.2	18 46 07.15	±0.8	−01 51 56.5	±1.1	111.4	140.1	5.22	6.56	0.37
OH 32.0−0.5	18 48 51.21	±0.8	−01 07 29.3	±0.6	55.0	96.0	8.3	5.1	0.4
OH 32.1+0.9	18 44 04.62	±0.8	−00 20 29.9	±0.6	124.7	149.3	2.36	3.77	0.17
OH 34.9+0.8	18 49 43.87	±1.1	+02 00 08.0	±0.7	54.0	82.9	2.39	3.10	0.11
OH 36.4+0.3 A	18 54 01.52	±0.6	+03 16 08.2	±0.6	83.5	121.1	4.88	2.76	0.19
OH 36.4+0.3 B	18 53 57.61	...	+03 13 21.1	...	...	...	...	...	...
OH 36.4+0.3 C	18 54 07.15	...	+03 14 02.1	...	...	...	...	...	...
OH 37.1−0.8	18 59 36.22	±0.8	+03 15 53.3	±1.1	75.0	101.5	14.41	20.32	0.47
OH 37.7−1.4	19 02 40.07	±0.3	+03 36 23.4	±0.6	100.0	119.9	2.32	0.47	0.16
OH 39.9−0.0	19 01 42.93	±0.6	+06 08 45.0	±0.8	133.7	163.0	3.6	6.2	0.4

* 1612 OH flux density at the time of the infrared observations; spectral resolution is 4.9 kHz.

TABLE 2

OH IR STARS IN THE GALACTIC CENTER REGION: ACCURATE RADIO POSITIONS, VELOCITIES, AND PEAK OH FLUX DENSITIES

Name (1)	R.A. (1950)[a] (2)	Decl. (1950)[a] (3)	LV (km s^{-1}) (4)	HV (km s^{-1}) (5)	S_{LV}[b] (Jy) (6)	S_{HV}[b] (Jy) (7)
OH 359.1+1.1	17^{h}35^{m}56.98	−29 02 24.8	−146.5	−128	2.3	2.8
OH 359.2+0.2	17 39 55.33	−29 29 36.1	−150	−121	0.9	2.0
OH 359.4+0.1	17 40 34.13	−29 24 59.5	−199	−223.5	0.8	2.2
OH 0.2+0.0	17 42 45.49	−28 44 10.0	+145	+174	1.1	0.7
OH 0.3−0.2	17 43 56.64	−28 43 41.2	−356	−327	2.3	1.9
OH 0.5−0.2	17 44 14.94	−28 35 31.8	+130	+153.5	0.9	1.5
OH 1.08+0.4	17 43 35.37	−27 48 47.2	−142	−108	<0.6	<0.6
OH 1.1−0.8	17 48 16.88	−28 24 52.7	−9	+30	20.6	24.5
OH 1.5−0.1	17 46 12.10	−27 41 00.8	−141.5	−114.5	2.7	5.1
OH 1.7−0.0	17 46 53.55	−27 24 10.0	−105	−134	0.8	3.5
OH 2.6−0.4	17 50 11.14	−26 56 01.5	−27	+18.5	13.3	14.2
OH 4.0+0.9	17 48 17.90	−25 01 08.7	+59	+88	1.3	1.0
OH 5.0−0.4	17 54 32.21	−25 12 42.6	−100	−146	1.8	2.5
OH 9.0−0.1	18 03 09.13	−21 14 02.4	−64	−33	<0.9	<0.9
OH 9.6+0.5	18 02 10.19	−20 22 30.6	−49	−76	2.0	3.5
OH 12.8−0.9	18 13 53.45	−18 16 08.9	−67	−44	9.7	2.3
OH 12.8+0.3	18 09 23.09	−17 43 45.1	+125	+152	<1.0	<1.0
OH 14.8+0.2	18 13 48.70	−16 05 15.0	+109	+133	<1.0	<1.0

[a] 3 σ uncertainties in R.A. = ±0^s.3 and in Decl. = ±0".9.

[b] 1612 MHz OH flux density on 1981 Aug 27–Sep 1; upper limits are 3 σ; spectral resolution is 4.9 kHz; 3 σ uncertainty is ±0.2 Jy.

been adopted for consistency with other published work. Limited UV coverage for OH 36.4+0.3 resulted in some uncertainty; position A is the most likely but two less plausible positions (B and C) are also given. The positions of OH 37.7−1.4, observed on both days, agreed within 0".2, confirming the accuracy of the measurements. Comparison with more recent VLA observations of some of the stars (Herman 1983) further strengthens our confidence in the results. For OH 20.7 and OH 31.0 the near-infrared positions listed by Jones, Hyland, and Gatley (1983) are more than 10" offset from our improved radio positions, suggesting that their infrared objects may not be associated with the OH masers.

Accurate positions for the galactic-center sample were determined with the VLA on 1981 May 7. At this time, by using a bandpass of 390 kHz and 64 autocorrelation channels of 6.1 kHz each, 13 telescopes could be employed, covering a range in baselines from 0.2 to 10.5 km. The synthesized beam was 7" × 4". Instrumental phase calibration was effected using the standard calibration source 1748−253 and the low-elevation, secondary calibration source 1741+038. The names of the stars and their radio positions are listed in Table 2 in columns (1), (2), and (3). The data on 1741−038 show that the positional uncertainty due to systematic phase errors is less than 0".1.

Single-dish OH fluxes of the tangential stars were measured with the Dwingeloo 25 m radio telescope in 1980, within 20–60 days of the Wyoming infrared observations (see § IIc). Since this time difference is much less than 10% of the typical periods for these stars (Herman 1983), the infrared and radio fluxes can be considered coeval. Fluxes for the galactic-center sample were measured with the 85 foot (26 m) telescope at Hat Creek between 1981 August 27 and September 1, one month after the infrared observations on the IRTF (see § IIc). No single-dish observations were made at the time of the UKIRT infrared observing run in 1982.

The high spectral resolution of the single-dish measurements (0.46 km s^{-1}) provided very accurate velocities and peak fluxes. Tables 1 and 2 contain the measured radio parameters of the two velocity components of the OH emission profiles for the tangential and the galactic-center samples respectively; radial velocities with respect to the local standard of rest, of the low- and high-velocity (LV, HV) peaks of the OH line profile are presented in columns (6) and (7) of Table 1 and columns (4) and (5) of Table 2; the corresponding peak flux densities, S_{LV} and S_{HV}, are shown in columns (8) and (9) of Table 1 and columns (6) and (7) of Table 2. The 1 σ uncertainty in the OH flux density measurement of the tangential sample is listed in the last column of Table 1.

c) *Infrared Observations*

Infrared observations of the tangential sources were made at the Cassegrain focus of the Wyoming Infrared Telescope (WIRO) in August, 1979 and 1980, using a helium-cooled bolometer (Bentley 1980). The aperture and chopper throw were 7".5 and 20" respectively. Infrared observations of the galactic-center sample were made at the IRTF and UKIRT on Mauna Kea, Hawaii, in 1981 July and 1982 June respectively, using the standard helium-cooled bolometers and also the liquid nitrogen–cooled InSb photometer at the UKIRT. A 6" aperture was employed at the IRTF and one of 7".5 at the UKIRT; chopper throws were 15" EW at IRTF and 30" in declination at UKIRT. Time did not allow us to observe all the stars in Table 2.

In general, measurements of the infrared counterparts of the OH IR stars were made by integrating on the VLA positions using a broad-band filter centered at 10 μm, where the energy distributions usually peak and where confusion by foreground K and M giants is negligible. However, for a few galactic-center sources, searches at UKIRT were carried out at 8.7 or 20 μm when the earlier IRTF observations had shown that either the 10 μm absorption feature was sufficiently strong to preclude a 10 μm detection or that the energy distribution peaked longward of 12.5 μm. Infrared positions determined for the stronger sources from a five-point grid centered on the VLA positions agreed well with the radio positions. Long integrations adjacent

TABLE 3

FILTER CHARACTERISTICS

WIRO		ZEROTH MAG	IRTF		UKIRT		ZEROTH MAG*
λ (μm)	$\Delta\lambda$ (μm)	F_ν (Jy)	λ (μm)	$\Delta\lambda$ (μm)	λ (μm)	$\Delta\lambda$ (μm)	F_ν (Jy)
2.3	0.7	598	...	...	...	...	...
3.6	1.2	277	3.8	0.67	3.8	0.65	238
4.9	0.7	158	4.8	0.57	4.8	0.60	153
8.7	1.0	54	8.7	1.19	8.7	1.2	50
...	...	...	9.8	1.0	9.7	1.0	40
10.0	5.8	41	10.3	1.03	10.3	1.25	34
11.4	2.0	32	11.6	1.26	11.6	1.17	28
12.6	0.8	26	12.5	1.17	12.5	1.25	24
19.5	5.8	12	2.0	9.0	20.9	6.0	10

* Applies to both UKIRT and IRTF.

to the radio positions of a few objects yielded no detections. We are therefore confident that the infrared sources can be identified unambiguously with the OH stars.

Following the detections of the IR counterparts, photometric measurements between 3 and 20 μm were made. Appropriate filter characteristics are presented in Table 3. After taking account of the relevant air-mass corrections, magnitudes at each wavelength were determined from comparison with standard stars. Conversion from magnitudes to flux densities was accomplished using the values shown in Table 3 (cf. Gehrz, Hackwell, and Jones 1974; Beckwith *et al.* 1976). The measured infrared flux densities and 3 σ upper limits for the tangential sample are given in Tables 4 and 5, while those for the galactic-center sample are in Table 6. In both tables, the year in which the observations were made is indicated in column (2). Corresponding infrared energy distributions are shown in Figures 1 and 2 respectively. For wavelengths between 3.8 and 12.5 μm the uncertainties in the fluxes are of order $\pm 10\%$, and at 20 μm about 15%. Typical error bars for the shorter wavelengths are plotted at the 8.7 μm data point in each source energy distribution. Error bars for the 20 μm flux are also indicated.

TABLE 5

UPPER LIMITS FOR TANGENTIAL STARS (1980 Observations)

Name	10 μm Flux Density (Jy)
OH 17.2.....	< 2.9
OH 18.5.....	< 2.5
OH 25.1.....	< 2.5
OH 27.0.....	< 3.2
OH 27.5.....	< 4.5
OH 29.4.....	< 4.0
OH 36.4.....	< 2.6
OH 37.1.....	< 3.1

III. RESULTS AND ANALYSIS

Long-term monitoring observations at 18 cm (Harvey *et al.* 1974; Jewell, Webber, and Snyder 1980; Herman 1983) show that L_{OH} and L_* change simultaneously, strongly suggesting that the OH maser is radiatively pumped. But from the observed correlation between L_{OH} and the shell size, and from the very broad OH luminosity distribution (cf. BHMW), BH have argued that L_{OH} is a steep function of the stellar mass-loss rate and more or less independent of L_*. This is also suggested by the observed correlation between L_{OH} and near-infrared colors (e.g., Jones, Hyland, and Gatley 1983; Engels 1982; Herman 1983). This raises the question of the relation between M and L_{OH}, and the nature of the underlying star. As a result of (1) homogeneity, (2) simultaneous radio and infrared observations, and (3) information at $\lambda > 10$ μm, the present sample allows a quantitative analysis of the data involving L_{OH}, L_*, and M and a better understanding of the influence of M on the maser pump efficiency. The physical parameters of the stars and their circumstellar shells, determined from the radio and IR observations described above, are summarized in Tables 7 and 8. Their derivation and the influence of extinction are discussed in Appendices A and B respectively.

a) *The* OH *Maser Flux and Stellar Luminosity*

L_{OH} ranges from 1–10 Jy kpc^2 for nearby, optically identified OH emitting Miras to 10–1000 Jy kpc^2 for the distant, OH

TABLE 4

INFRARED FLUX DENSITIES OF TANGENTIAL OH IR STARS (Jy)

NAME	DATE	WAVELENGTH (μm)							
		2.3	3.6	4.9	8.7	10.0	11.4	12.6	19.5
OH 10.8+1.5.....	1980	...	0.1	...	11.7	3.8	3.9	12.9	29.1
OH 18.2+0.5.....	1980	...	0.7	...	10.7	8.1	6.1	15.2	< 12.8*
OH 20.7+0.1.....	1979	...	< 0.2*	0.8	2.3	2.5	0.9	5.8	7.9
OH 21.5+0.5.....	1979	< 0.1*	2.1	20.6	35.0	29.2	16.7	63.4	68.5
OH 24.7−0.1.....	1979	0.9	11.6	27.7	30.5	24.5	22.0	33.6	28.3
OH 27.2+0.2.....	1979	0.2	2.2	5.0	8.3	7.8	8.8	10.7	9.2
OH 27.8−1.5.....	1980	3.2	14.7	...	38.8	37.7	37.2	38.6	31.6
OH 28.5−0.0.....	1980	...	0.3	...	6.5	7.4	...	< 6.8*	...
OH 30.1−0.7.....	1979	< 0.1*	1.4	16.9	68.6	53.6	28.7	100.5	129.4
OH 31.0−0.2.....	1980	...	< 0.2*	...	19.8	14.1	< 14.7*	24.8	19.4
OH 32.0−0.5.....	1979	< 0.1*	0.1	2.8	5.9	6.4	3.9	13.6	15.6
OH 32.1+0.9.....	1980	0.1	1.5	...	12.0	< 7.0*	...	11.4	...
OH 34.9+0.8.....	1980	< 0.1*	1.8	...	10.1	6.6	...	10.3	...
OH 37.7−1.4.....	1980	< 0.1*	1.1	3.7	7.1	8.3	...	< 5.4*	...
OH 39.9−0.0.....	1979	< 0.1*	1.1	4.9	11.6	9.2	6.8	15.4	15.6

* Upper limits are 3 σ.

TABLE 6

INFRARED FLUX DENSITIES OF OH IR SOURCES IN THE GALACTIC CENTER (Jy)

NAME	DATE	WAVELENGTH (μm)							
		3.8	4.8	8.7	9.7	10.5	11.5	12.5	19.8
OH 359.1 + 1.1	1982	< 0.2ª	0.08	0.31	0.34	...	...	1.04	3.13
	1981	...	0.11	0.61	0.73	0.79	1.61	2.33	10.67
OH 359.4 + 0.1	1982	...	...	< 0.2ª	...	...	...	0.45	< 1.6ª
	1981	...	0.23	0.52	0.27	...	0.56	1.87	2.21
OH 0.2 + 0.0	1982	0.95	1.24	1.73	0.38	0.31	1.73	1.85	2.60
	1981	...	0.58	0.47	0.09	< 0.2ª	0.60	0.5	0.50
OH 0.3 − 0.2	1981	...	...	...	...	...	...	0.45	1.2
OH 0.5 − 0.2	1982	...	0.33	0.70	< 0.4ª	...	0.73	1.10	1.27
	1981	...	0.51	1.04	0.24	0.29	1.18	3.13	3.2
OH 1.08 + 0.4	1981	...	< 0.3ª	...	...	< 0.2ª	...	0.23	4.2
OH 2.6 − 0.4	1982	78.09	80.30	197.23	159.24	167.29	191.94	112.78	167.49
OH 4.0 − 0.9	1982	...	< 0.2ª	0.63	0.84	...	...	< 2.1ª	5.25
OH 4.6 − 0.4	1982	3.60	4.93	8.53	1.36	1.63	7.78	9.91	8.95
	1981	...	6.44	8.06	2.11	2.33	9.23	17.42	23.3
OH 9.6 + 0.5	1982	7.88	6.44	18.32	14.93	15.40	11.83	15.43	15.85
	1981	...	5.93	16.72	19.23	17.88	19.52	19.08	17.0

ª Upper limits are 3 σ.

luminous, but optically obscured, OH IR stars studied in this paper. The OH luminosity of these objects increases steeply with decreasing L_{OH}, and it has been suggested that Miras may represent the low-luminosity tail (BHMW). Values of L_* for Miras and OH IR stars are not significantly different, leading to the hypothesis that L_{OH} is independent of L_* (BH). Indeed, the present data support this contention; in Figure 3, where the tangential sources are plotted as filled circles and the galactic-center sample is represented by crosses, there is no evidence of a strong correlation between L_{OH} and L_*.

L_{OH} for the galactic-center sample is a factor of 2 to 3 smaller than that for the tangential sample, reflecting the higher sensitivity of the OH observations near the galactic center. The mean bolometric luminosity for the detected stars in the tangential sample is $3.4 \times 10^4\ L_\odot$, whereas it is $2 \times 10^3\ L_\odot$ for the stars in the vicinity of the galactic center ($l < 1°$). It is not clear whether this discrepancy is real. It could result from differences in the sensitivity and completeness of each sample or from the variations between the space density of OH IR stars near the galactic center and in the disk near tangential point. Although OH IR stars in the galactic center have much lower bolometric luminosities than those at the tangential point, a larger interstellar extinction toward the galactic center could to some extent explain the disparity. It is, however, unlikely that it can account for a discrepancy of more than a factor of 2, indicating that the OH IR stars in the bulge are intrinsically at least 5 times less luminous than those in the disk.

Figure 4 demonstrates that there is no correlation between L_{OH} and v_e, the shell expansion velocity. Given the absence of a correlation in Figure 3, this is scarcely surprising because, for OH IR stars, v_e is statistically related to the main-sequence mass (BHMW). Since the main-sequence mass is related to the AGB mass (cf. Iben 1981), which in turn determines the bolometric luminosity (Paczyński 1970), v_e and L_* should in fact be correlated. The statistical data of Jones, Hyland, and Gatley (1983) appear to support such a correlation and, although the scatter in Figure 5 is large, there is a weak trend for the most luminous stars to have higher values of v_e.

b) *The OH Maser Flux and the Circumstellar Dust Density*

The long-term variability and bolometric luminosity of these OH IR stars suggest that their stellar parameters are similar to those of the OH emitting Miras with effective temperatures between 2500 and 3500 K and maxima in the energy distributions between 1 and 2 μm (cf. Merrill 1977). It is commonly thought that the OH maser is pumped by 35 μm photons (Elitzur, Goldreich, and Scoville 1976), but in the case of the OH luminous OH IR stars, the stellar photospheric flux at 35 μm is clearly insufficient to provide enough maser pump photons. This implies that the maser luminosity depends on the efficiency with which the stellar light is converted to 35 μm emission in the circumstellar shells, i.e., on the dust-column density. If the pumping is due to 35 μm photons and the maser is saturated, then stars with the same OH luminosity but different values of L_* produce similar 35 μm fluxes, and the energy distributions must be redder and cooler for lower values of L_*. Thus the ratio L_{OH}/L_* should be positively correlated with the fraction of the total energy that is emitted at 35 μm.

In Figure 6 L_{OH}/L_* is plotted against the fraction of the total energy emitted at 20 μm, $\lambda F_{20}/F_{IR}$. Since in most cases the maximum in the energy distribution of these objects lies shortward of 35 μm, $\lambda F_{20}/F_{IR}$ is a reasonable measure of the relative amount of energy emitted at 35 μm. Both L_{OH}/L_* and $\lambda F_{20}/F_{IR}$ are distance-independent. The OH luminosity increases steeply with the fraction of the total emission that emerges at 20 μm, that is, when the energy distribution becomes redder. It is clear from this figure that for most stars there is a remarkably tight correlation between the two quantities, which is intrinsic and cannot be due to variable interstellar extinction. Three objects, OH 359.1, OH 4.6, and OH 10.9, which lie significantly below the observed correlation, have anomalously low OH luminosities. OH 0.2 lies well above the trend and appears to emit more OH photons than 35 μm pump photons, in violation of the simple 35 μm pump model (Elitzur, Goldreich, and Scoville 1976). This discrepancy is discussed in § IV.

A linear regression fit, excluding the four anomalous sources

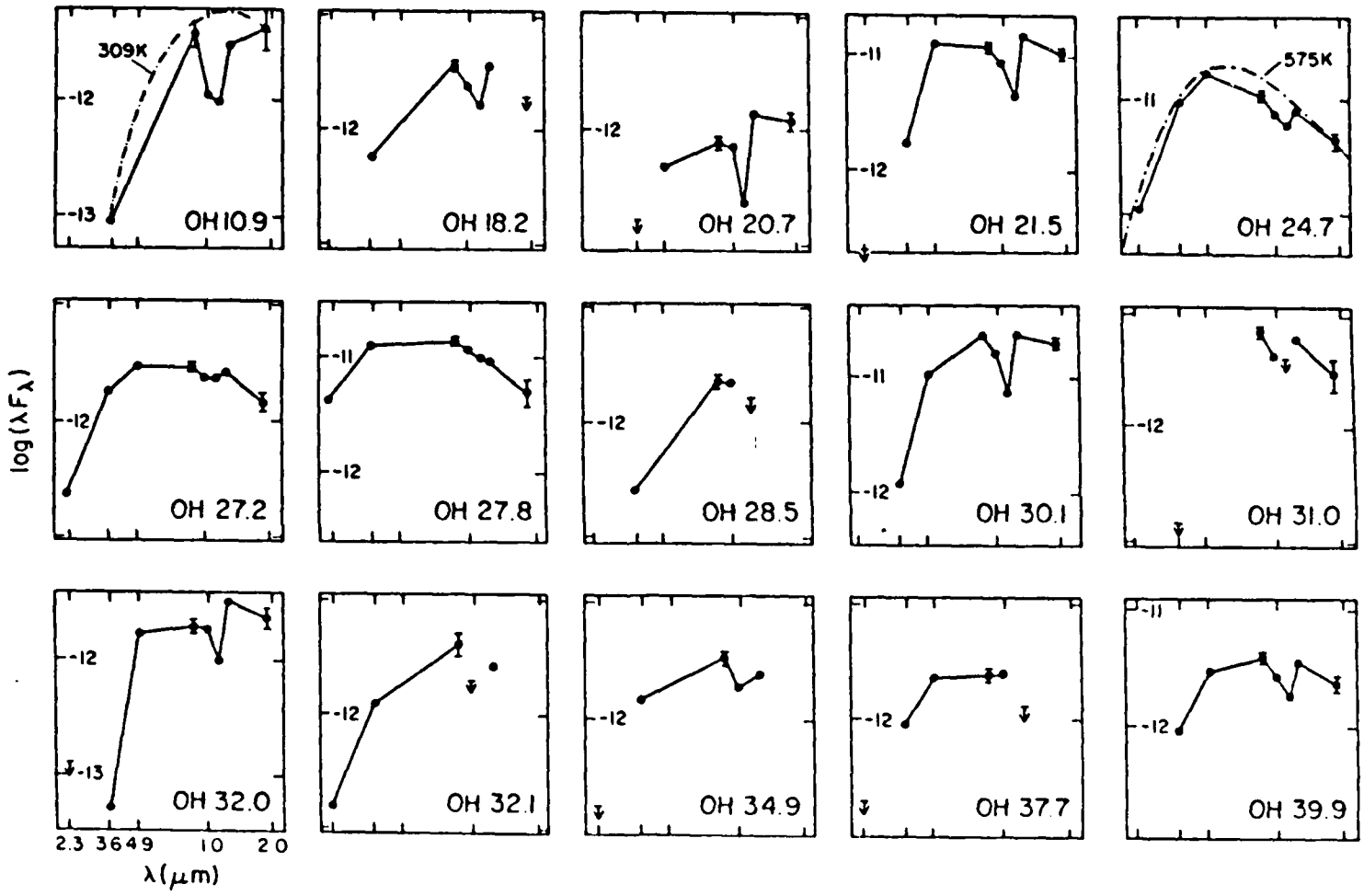

FIG. 1.—Infrared energy distributions of the tangential OH IR stars measured at WIRO. The flux scale is in units of W m^{-2}. Upper limits are indicated by an arrow, uncertainties by a bar at the 8.7 and 20 μm points. Examples of a blackbody fit are given for OH 10.9 and OH 24.7.

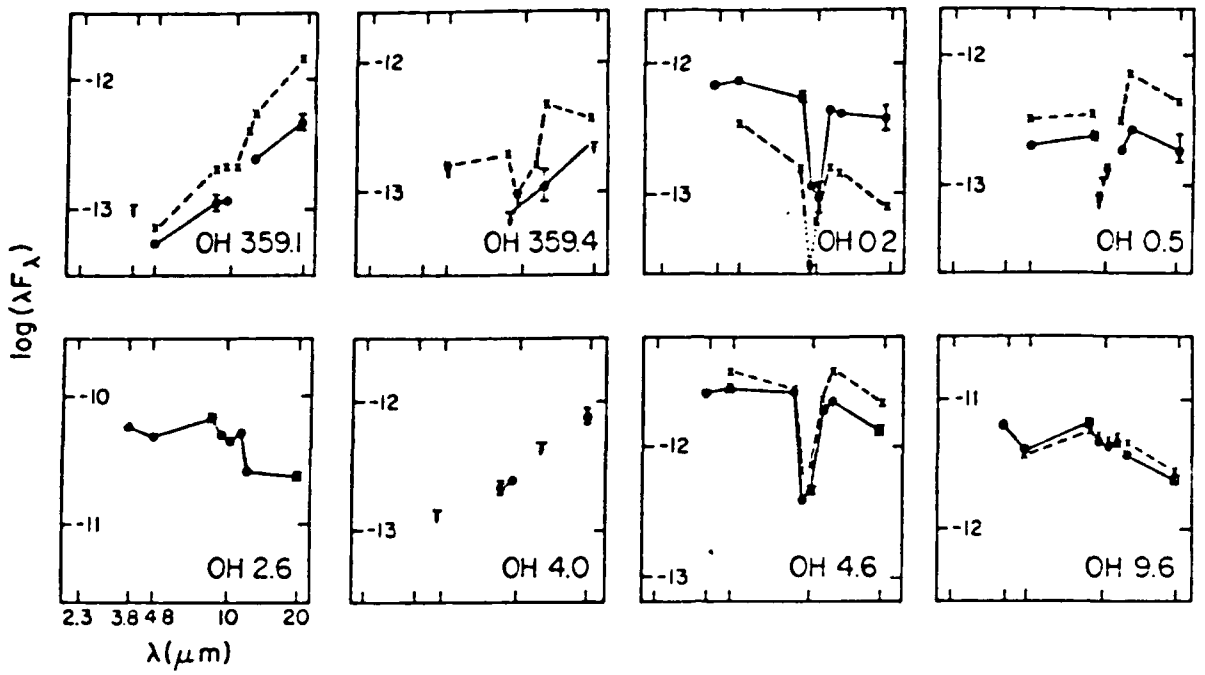

FIG. 2.—Infrared energy distributions of the galactic center sample measured with IRTF in 1981 (*continuous*) and with UKIRT in 1982 (*dashed*)

and the upper limit for OH 18.2, yields

$$\log\left(\frac{L_{OH}}{L_\odot}\right) = 2.4(\pm 0.1)\log\left(\frac{\lambda F_{20}}{F_{IR}}\right) - 0.5(\pm 0.03)\,. \quad (1)$$

The harmonic mean OH flux, S_{OH}, is then given by

$$S_{OH} = 0.9 F_{IR}\left(\frac{\lambda F_{20}}{F_{IR}}\right)^{2.4}\ \text{Jy}\,, \quad (2)$$

with F_{IR} and λF_{20} in units of 10^{-13} W m^{-2}. The dependence of S_{OH} on F_{IR} and λF_{20} F_{IR} is consistent with the observations; the OH maser output follows closely the time variations in $L_\odot$, as would be expected from $S_{OH} \propto F_{IR}$. In addition, the steep dependence of S_{OH} on λF_{20} F_{IR} implies that no direct correlation is expected between $L_\odot$ and L_{OH} (cf. Fig. 3); the relative amount of long-wavelength flux, which is a function of the dust-column density and hence the mass-loss rate, rather than

TABLE 7

RADIO AND INFRARED PROPERTIES OF TANGENTIAL OH IR STARS

Name	Distance[a] (kpc)	L_{OH}[a] (Jy kpc^2)	v_e (km s^{-1})	F_{IR} (10^{-13} W m^{-2})	$L_\odot$[a] (10^4 $L_\odot$)	T_c (K)	τ_{at}
OH 10.9+1.5.....	8.5–11.8	120–230	16.25	63 ± 7	1.34–2.58	310	1.3
OH 17.2−1.1.....	9.6	240	12.50	...	...	...	...
OH 18.2+0.5.....	9.5	150	12.15	50 ± 6	1.33	410	0.9
OH 18.5+1.4.....	9.5	620	10.65	...	...	...	...
OH 20.7+0.1.....	9.4	720	18.30	18 ± 2	0.47	350	1.8
OH 21.5+0.5.....	8.6–10.1	2170–2990	18.20	260 ± 30	5.68–7.83	410	1.2
OH 24.7−0.1.....	9.1	220	16.50	265 ± 30	6.48	580	0.4
OH 25.1−0.3.....	9.1	590	12.40	...	...	...	...
OH 27.0−0.4.....	7.4–10.4	300–590	14.60	...	...	...	...
OH 27.2+0.2.....	6.7–11.1	90–260	19.40	60 ± 7	0.80–2.18	520	0.2
OH 27.5−0.9.....	8.9	520	13.50	...	...	...	...
OH 27.8−1.5.....	6.1–11.6	90–340	15.20	340 ± 40	3.73–13.5	620	<0.1
OH 28.5−0.0.....	8.8	900	13.35	49 ± 6	1.12	>380	...
OH 29.4−0.8	8.7	590	11.85	...	...	...	...
OH 30.1−0.7.....	7.3–10.0	3110–5840	20.30	380 ± 45	5.98–11.2	360	1.2
OH 31.0−0.2.....	8.6	430	14.35	96 ± 10	2.10	<340	>0.4
OH 32.0−0.5.....	5.4–11.6	190–880	20.50	45 ± 5	0.39–1.79	410	1.0
OH 32.1+0.9.....	8.5	220	12.30	75 ± 9	1.60	500	...
OH 34.9+0.8.....	4.8–11.6	60–370	14.45	56 ± 7	0.38–2.22	490	0.5
OH 36.4+0.3.....	8.1	240	18.85	...	...	...	...
OH 37.1−0.8.....	8.0	240	13.25	...	...	...	...
OH 37.7−1.4.....	7.9	70	10.00	56 ± 7	1.03	>490	...
OH 39.9−0.0.....	7.7	280	14.65	70 ± 8	1.23	430	0.8

[a] In case of a distance ambiguity, values for both the near- and the far-kinematic distance are given.

TABLE 8

RADIO AND INFRARED PROPERTIES OF THE GALACTIC CENTER OH IR STARS

Name	Distance (kpc)	L_{OH} (Jy kpc^2)	v_e (km s^{-1})	F_{IR} (10^{-13} W m^{-2})	L_* (10^4 $L_\odot$)	T_c (K)	τ_{sil}	Year
OH 359.1	10	...	9.25	5.4	0.16	340	...	1982
		250	...	12.6	0.37	300	0.2	1981
OH 359.4	10	...	12.25	<1.4	<0.04	<230	...	1982
		130	...	<4.5	<0.13	<370	>1.0	1981
OH 0.2	10	...	14.5	11.9	0.34	590	1.6	1982
		90	...	3.4	0.1	450	2.1	1981
OH 0.3	10	210	14.5	>1.2	>0.04	...	...	1981
OH 0.5	10	...	11.75	3.8	0.11	460	>0.8	1982
		120	...	8.1	0.24	400	>1.7	1981
OH 1.08	10	<60	17.0	<4.8	<0.14	...	...	1981
OH 2.6	5	340[a]	22.75	936	6.8	600	0.2	1982
OH 4.0	10	110[a]	14.5	<6.6	<0.19	370	...	1982
OH 4.6	10	...	23.0	56	1.6	530	1.8	1982
		210	...	89	2.6	500	1.6	1981
OH 9.6	10	...	23.5	90	2.6	500	0.2	1982
		260		98	2.9	460	<0.1	1981

[a] 1981 measurement.

the integrated flux (stellar luminosity), is the dominant parameter governing the maser flux. That is to say, the OH luminosity depends mainly on the effective temperature of the circumstellar dust (see § IIIc), with an overall scaling factor due to the bolometric luminosity. Since the precise relation between the relative amount of 20 μm flux and M is not known, a direct comparison between L_{OH} L_* and M is not possible.

c) Silicate Absorption

The silicate absorption feature at 9.7 μm is formed in the cool outer regions of the circumstellar shell. Its apparent depth, τ_{sil}, is a measure of the dust-column density and is also expected to be inversely proportional to T_c (Kwan and Scoville 1976). Since τ_{sil} appears to be correlated with L_{OH} L_* (Herman 1983), it should increase with λF_{20} F_{IR}; Figure 7*a* shows that this is indeed the case, although OH 0.2 and OH 4.6 have unexpectedly high values of τ_{sil}. Both objects are also anomalous in Figure 5. OH 359.1 is extremely red but has a low value of τ_{sil}, similar to OH 17.7−2.0 (Olnon *et al.* 1984), suggesting that in the coolest objects, which presumably experience the largest mass-loss rate, the formation of the silicate feature is severely inhibited by an as yet unspecified mecha-

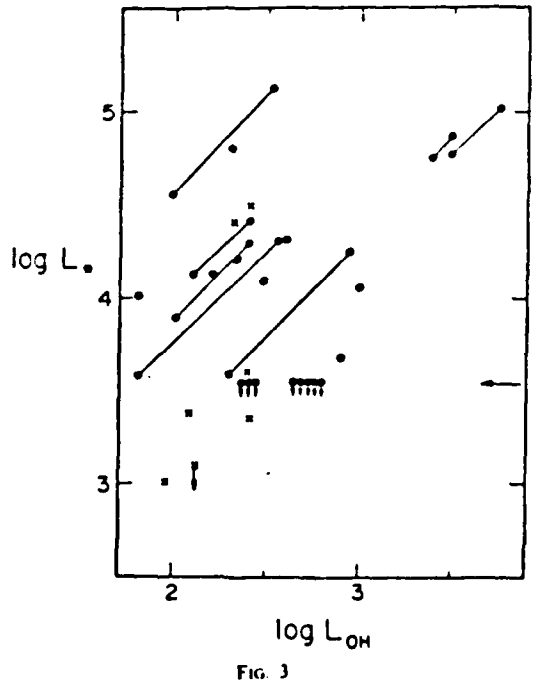

FIG. 3

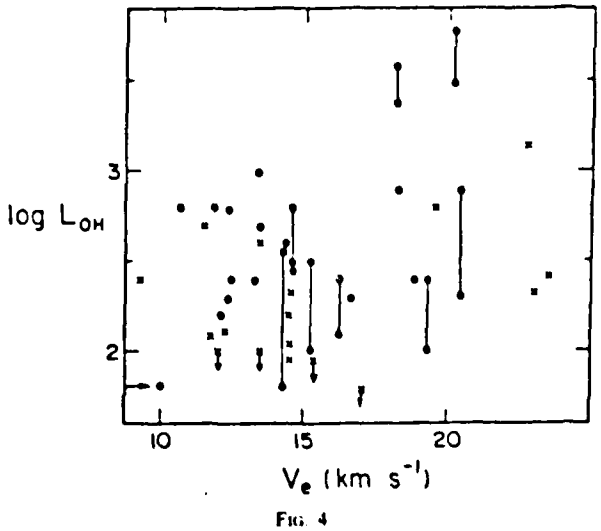

FIG. 4

FIG. 3.—The stellar bolometric luminosity L_* in $L_\odot$ as a function of the maser luminosity L_{OH} in Jy kpc^2. In this and the following figures the tangential sample is indicated by filled circles, the galactic-center sample by crosses. Values corresponding to the near- and far-kinematic distances for the tangential sample are connected by a line. The arrow indicates the sensitivity limit for the WIRO measurements (see text).

FIG. 4.—The maser luminosity as a function of v_e, the outflow velocity of the circumstellar shell.

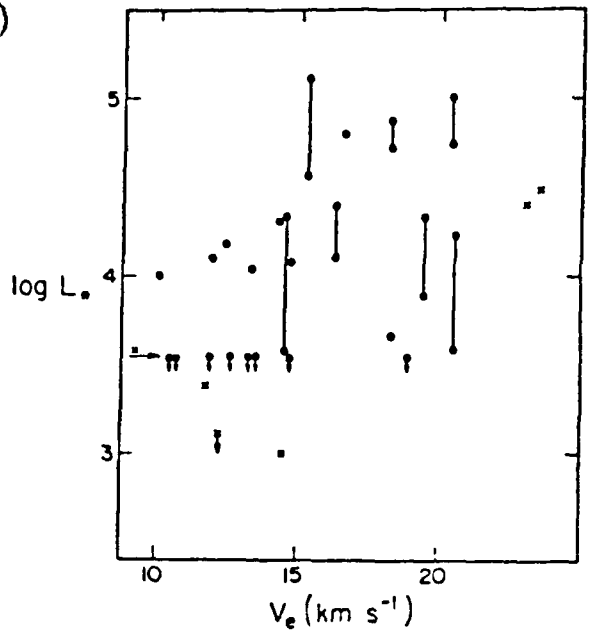

FIG. 5

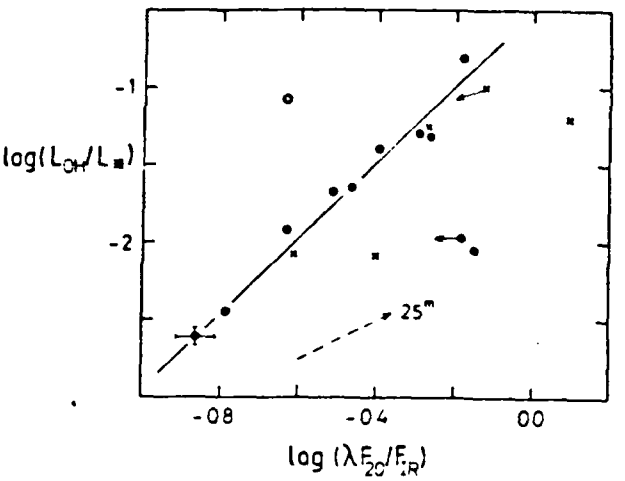

FIG. 6

FIG. 5.—Bolometric luminosity as a function of outflow velocity

FIG. 6.—The ratio of maser to bolometric luminosity as a function of the fraction of total infrared energy emitted at 20 μm. The open circle represents OH 0.2 (see text). L_{OH} and L_* are in the same units as in Fig. 3. Infrared energies are in W m^{-2}. The dashed arrow indicates the effect of 25 mag of visual extinction (see Appendix). The solid line is a least-squares fit through the tangential sample, excluding the anomalous sources (see eq. 1). Typical error bars are indicated.

nism. A linear fit through all data points except the limits and the two anomalous stars gives the following relation:

$$\tau_{sil} = 2.1(\pm 0.2) \log\left(\frac{\lambda F_{20}}{F_{IR}}\right) + 1.8(\pm 0.2), \qquad (3)$$

with a correlation coefficient of 92%. Figure 7*b* confirms that the silicate optical depth is proportional to T_c^{-1}.

An interstellar component in the silicate absorption feature has not yet been completely ruled out. In a small sample of OH IR stars Evans and Beckwith (1977) found no correlation between τ_{sil} and distance, arguing for a circumstellar origin. If the silicate feature were due solely to interstellar extinction, no correlation with $\lambda F_{20}/F_{IR}$ would be seen in Figure 7*a* and, indeed, τ_{sil} would be expected to depend on galactic latitude. Since this is not the case, the possibility of the silicate feature arising in the interstellar medium can be ruled out.

IV. DISCUSSION

Our simultaneous radio and infrared observations of two samples of distant OH IR stars at the tangential point and the

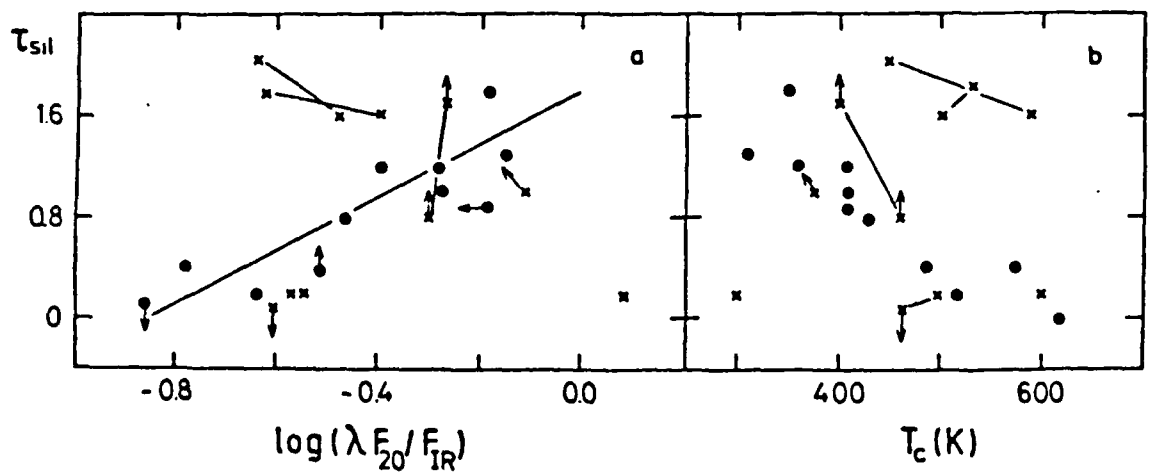

FIG. 7.—The apparent silicate optical depth as a function of (*a*) the fraction of infrared energy emitted at 20 μm and (*b*) the color temperature between 4.8 and 12.5 μm. The solid line in (*a*) is a least-squares fit to the tangential sample (see eq. 3).

galactic center demonstrate that the OH luminosities of these objects are dependent on the fraction of the total infrared energy which is emitted near 35 μm, which in turn is a measure of the mass-loss rate. Sources with the same stellar parameters, such as bolometric luminosity and mass, may have widely different circumstellar properties. This is reflected in large variations in L_{OH} among stars with similar values of v_e and L_*. For a given bolometric luminosity, stars with higher OH luminosity have redder infrared energy distributions and deeper silicate absorption features, indicative of cooler circumstellar shells and higher mass-loss rates.

a) *Maser Pump Efficiency*

Equations (1) and (2) show that for a given star L_{OH} is a function of the relative amount of long-wavelength photons produced in the circumstellar shell. In the 35 μm pumping scheme the observed maser pump efficiency ϵ is given by

$$\epsilon = \frac{S_{OH}}{S_{35}} A_{35} \frac{\Omega_{OH}\delta v_{OH}}{\Omega_{35}\delta v_{IR}}$$

(cf. Evans and Beckwith 1977), where S, Ω, and δv are the flux densities, the solid angles into which the flux is emitted, and the bandwidths in km s^{-1} for OH emission and 35 μm absorption respectively, and A_{35} is the interstellar attentuation. In the simplest case, the last three factors are 1 and the predicted efficiency for a saturated maser, given by the flux density ratio, is 0.25 (Elitzur, Goldreich, and Scoville 1976).

For the present stars S_{35} was estimated from a linear extrapolation between 12 and 20 μm. The derived ratio S_{OH}/S_{35} is plotted in Figure 8 against $\lambda F_{20}/F_{IR}$. Given the uncertainties, the flux-density ratio, reflecting the efficiency, is generally close to the expected value of 0.25. Nevertheless, there is some indication of a trend for the flux-density ratio to increase from 0.15 to 0.6 with increasing circumstellar reddening, suggesting a corresponding increase in the observed pump efficiency. This can be reconciled with the expected value $\epsilon = 0.25$, if the bandwidth ratio $\delta v_{OH}/\delta v_{35}$ decreases with increasing thickness of the circumstellar shell. When the shell becomes thicker, the radius at which the majority of 35 μm pump photons are produced grows, and δv_{35} increases due to the changing geometry between the maser-emitting region and the 35 μm pump region (cf. Evans and Beckwith 1977).

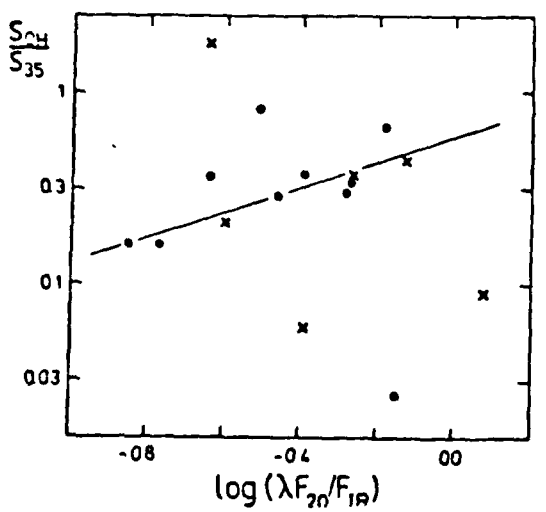

FIG. 8.—The ratio of OH to 35 μm flux as a function of the fraction of the infrared energy emitted at 20 μm.

b) *Variations in the Silicate Absorption Depth*

Our results also indicate that, for a given star, as L_* declines, an increase in the silicate absorption feature τ_{sil} should result. While the luminosity of the OH maser changes in phase with the bolometric luminosity of the central star, the amplitude of the variation is about a factor of 2 smaller (e.g., Herman 1983), with

$$\frac{F_{max}}{F_{min}} = 2\,\frac{S_{max}}{S_{min}}, \qquad (4)$$

where $S_{max,\,min}$ and $F_{max,\,min}$ are respectively the OH and bolometric fluxes at the maximum and minimum of the light curve. Thus, the relative amount of 35 μm flux, which reflects the temperature of the outer dust shell, should change as a function of phase in the light curve. Since the depth of the silicate feature indicates a temperature gradient between the regions where the 10 μm continuum and silicate features arise (Kwan and Scoville 1976), τ_{sil} should also vary over the light curve. From equations (2) and (4) it can be shown that

$$\left(\frac{\lambda F_{20}}{F_{IR}}\right)_{max} = 0.75\left(\frac{\lambda F_{20}}{F_{IR}}\right)_{min}. \qquad (5)$$

Thus, combining equations (5) and (3), the change in the silicate optical depth between minimum and maximum of the light curve is given by

$$\Delta\tau = \tau_{min} - \tau_{max} \approx 0.26,$$

where $\tau_{min,\,max}$ are the silicate optical depths at minimum and maximum light. Because of the large width of the 10 μm filter used at WIRO, the precise value of $\Delta\tau$ is uncertain, but effectively the relation implies that the silicate optical depth is smaller at maximum light than at minimum and should increase with decreasing L_*. This is in good qualitative agreement with our observations of those stars in the galactic-center sample for which infrared fluxes were measured at two epochs (cf. Fig. 2 and Table 6) and with the measurements of the bright OH IR star OH 26.5 + 0.6 (Forrest *et al.* 1978).

c) *Circumstellar Shell Size and OH Luminosity*

The correlation found between L_{OH} and the size of the circumstellar shell by BH can now be understood. As the mass-loss rate increases, the circumstellar shell density rises so that the OH maser can operate at larger radii from the star; the minimum density required for a saturated maser, $n_H = 10^4$ (cf. Elitzur, Goldreich, and Scoville 1976) is found over a greater surface area. Since the stimulated-emission rate for a saturated maser is determined by the number of pump photons, L_{OH} will not be enhanced merely by enlarging the maser volume. Nevertheless, with rising density the circumstellar dust becomes cooler and more stellar emission is converted to 35 μm flux. Thus, with increasing mass-loss rate, the effects of a higher number of pump photons and of available OH molecules combine to produce enhanced maser emission and keep the maser saturated.

V. CONCLUSIONS

In this paper we have presented simultaneous OH and infrared measurements of a homogeneous sample of OH IR stars at

the tangential point and near the galactic center; their distances are therefore well known. Very accurate radio positions, derived from VLA observations, and identifications of the infrared counterparts at wavelengths longward of 8 μm reduce the possibility of confusion. We find that the characteristics of the objects in each sample are very similar in most respects. Although there is some tendency for the luminosities of the galactic-center stars to be lower than those at the tangential point, the paucity of objects makes it difficult to ascertain whether this is significant. Future studies, perhaps based on the results of the IRAS survey, should make it possible to verify whether a population of low-luminosity masers indeed exists in the galactic bulge.

As a result of the homogeneity of the samples, the reliability of the infrared identifications, and the simultaneous radio and infrared measurements, it has been possible to establish a number of relations between various stellar and circumstellar properties. In particular, it has been shown quantitatively that the OH luminosity is dominated by the fraction of the infrared energy emitted longward of 20 μm and thus by the stellar mass-loss rate. However, L_{OH} is to some extent dependent on the bolometric luminosity so that, as observed, time variations in L_* are reflected in L_{OH}. It has also been demonstrated that the apparent optical depth of the silicate feature τ_{si} is determined by the stellar mass-loss rate, confirming that this feature arises in the circumstellar shell. Moreover, using the dependence of both L_{OH} and τ_{si} on the stellar mass-loss rate, and the fact that the amplitude of variability of the OH maser emission is half that of the stellar emission, the observed variations in τ_{si} over the light curve of a given object can be explained in a qualitative manner.

Our new data have permitted an investigation of the maser pump efficiency. Within the uncertainties, this is found to be consistent with the canonical value of 0.25. However, some tendency for the inferred efficiency to increase with increasing circumstellar reddening is discernible in the data.

The results discussed above were derived from a sample of stars covering a wide range of masses and luminosities. Although these objects represent the high-luminosity tail of the OH luminosity distribution, it seems justifiable to extend our conclusions to the majority of OH IR stars. In particular, it is clear that sources whose stellar properties are the same can have a variety of circumstellar attributes. In effect, for a given L_* a large range of values of L_{OH}, which reflect differing mass-loss rates, is possible. Thus these stars can be interpreted as representing an evolutionary sequence of increasing mass-loss rate.

The measurements described here were made at six observatories in the course of seven observing runs. As a result, thanks are due to many people for their contributions to the success of the project. We are grateful to the staff of WIRO for providing observing time and for their willing and competent assistance. At the IRTF and UKIRT, R. Isaacman helped with the observations. In particular we thank I. Gatley for his support at the UKIRT. J. Herman kindly made observations for us at Dwingeloo. At Hat Creek, M. Stevens most ably carried out the measurements, while the VLA results were made possible with help from A. Rots, J. Dreher, and R. Perley. Especially, we would like to thank J. Turner and S. Kulkarni, who carried out a major part of the VLA spectral-line data reduction. We are grateful to N. Scoville for a critical reading of the manuscript and to the referee, T. J. Jones, for helpful comments. This work was begun while one of us (B. B.) was at the Radio Astronomy Laboratory at U.C. Berkeley and was supported by NSF grant AST78-21037; J. Welch is thanked for his help and encouragement. A. I. S. is supported by NSF grant AST 82-10828 to the Owens Valley Radio Observatory.

APPENDIX A

DERIVED PHYSICAL PARAMETERS FOR OH IR STARS

The *distance* to the OH IR stars studied here, D, is based on a galactic distance scale, center-to-Sun, of $R_\odot = 10$ kpc. For the tangential sample it is derived kinematically from the stellar radial velocity $v = (HV + LV)/2$ (km s^{-1}) (where HV and LV are the velocities with respect to the local standard of rest of the high- and low-velocity components of the OH profile), using the galactic rotation curve of Burton and Gordon (1978). For stars with radial velocities larger than the maximum velocity allowed by circular rotation v_{max}, D is presumed equal to the distance to the tangential point. Stars with $v < v_{max}$ probably lie between the listed near- and far-kinematic distances. For the galactic-center sample, stars within a degree of the center have high radial velocities ($|v| > 100$ km s^{-1}) and are assumed to be part of the bulge population at a distance of 10 kpc (Habing *et al.* 1983). At $l > 1°$, where the density of the bulge drops off significantly, distances are more uncertain. Objects with small radial velocities ($|v| \leq 10$ km s^{-1}) are probably foreground stars and are assumed to be at the location of the molecular ring at 5 kpc distance, where the density distribution of the OH IR stars peaks (cf. BHMW). The remainder of the sample, with high negative or positive radial velocities, is assumed to be at a distance of $10 \pm 10l$ kpc, where l is the source galactic longitude in radians.

The *expansion velocity* of the circumstellar shell is $v_e = (HV - LV)/2$ (km s^{-1}).

The *OH luminosity* L_{OH} at 1612 MHz is $L_{OH} = D^2(S_{LV}\,S_{HV})^{1/2}$ (Jy kpc^2), where D is in kpc (cf. BHMW). The 3 σ sensitivity limit of the Dwingeloo and Onsala survey, from which the tangential sample was drawn, is $\sim$0.6 Jy. At a mean distance of 8.9 kpc this corresponds to a minimum detectable OH luminosity of 50 Jy kpc^2 and to a completeness limit of 100 Jy kpc^2. For the galactic-center sample, similar values apply.

Regarding *stellar luminosity*, most energy distributions in Figures 1 and 2 rise between 3 and 8.7 μm and many appear to be broader than expected for a single-temperature Planck curve, indicating the presence of circumstellar dust at different temperatures. The stellar radiation, which peaks around 1–2 μm, is absorbed by the dense dust shell and reemitted at longer infrared wavelengths. The integrated infrared flux F_{IR} determined from the observed energy distribution, and including a correction factor of 25% to account for flux emitted beyond 25 μm (cf. Werner *et al.* 1980), is therefore a good measure of the bolometric luminosity of the star.

The stellar luminosity is then $L_* = 2.9D^2F_{IR}$ ($L_\odot$), where D is in kpc and F_{IR} is in 10^{-13} W m^{-2}. If the OH sources without infrared detections (Table 5) have energy distributions similar to those detected, their 10 μm upper limits correspond to $L_* \leq 3.5 \times 10^3\ L_\odot$ for a mean distance of 8.9 kpc.

The *color temperature* T_c for each source was determined by fitting a Planck curve to the observed infrared energy distribution between 4.8 and 12.5 μm.

As for *silicate absorption*, the optical depth of the silicate feature τ_{sil} seen at 9.7 μm in Figures 1 and 2 was derived from the ratio of the measured flux at the deepest point of the feature λF_{sil} to the continuum flux at the same wavelength λF_{cont}, interpolated from the 8.7 and the 12.6 μm flux measurements, so that $\tau_{sil} = -\ln(\lambda F_{sil}/\lambda F_{cont})$.

APPENDIX B

THE EFFECTS OF INTERSTELLAR EXTINCTION

Stellar parameters, such as the bolometric luminosity and the color temperature, which are derived from the infrared observations, will be influenced by interstellar extinction. This can range from 7 to 32 mag in the visual for these distant stars (de Jong 1983). Using the extinction law in the infrared from Becklin *et al.* (1978), we calculate that for an average visual extinction of 20–30 mag the observed luminosity of a 400 K blackbody will be underestimated by a factor of $\sim$1.6. Since both distance uncertainties and variations in the extinction with respect to the mean could cause uncertainties in the derived bolometric luminosities of a factor of 2–3 for individual objects, no corrections for interstellar extinction were made. However, the influence of 25 mag of extinction on a blackbody of 400 K is shown in Figure 3 by an arrow. None of the trends discussed in the body of the text appear to be significantly influenced by interstellar extinction.

REFERENCES

Baud, B., and Habing, H. J. 1983, *Astr. Ap.*, 127, 73 (BH)
Baud, B., Habing, H. J., Matthews, H. E., and Winnberg, A. 1979a, *Astr. Ap. Suppl.*, 35, 179.
———. 1979b, *Astr. Ap. Suppl.*, 36, 193.
———. 1981, *Astr. Ap.*, 95, 156 (BHMW).
Becklin, E. E., Matthews, K., Neugebauer, G., and Willner, S. P. 1978, *Ap. J.*, 220, 831.
Beckwith, S., Evans II, N. J., Becklin, E. E., and Neugebauer, G. 1976, *Ap. J.*, 208, 390.
Bentley, A. F. 1980, Ph.D. thesis, University of Wyoming.
Bowers, P. F. 1978, *Astr. Ap.*, 64, 307.
Burton, W. B., and Gordon, M. A. 1978, *Astr. Ap.*, 63, 7.
de Jong, T. 1983, *Ap. J.*, 274, 252.
Elitzur, M., Goldreich, P., and Scoville, N. 1976, *Ap. J.*, 205, 384.
Enxeis, D. 1982, Ph.D. thesis, Bonn.
Evans, N. J., and Beckwith, S. 1977, *Ap. J.*, 217, 729.
Forrest, W. J., *et al.* 1978, *Ap. J.*, 219, 114.
Gehrz, R. D., Hackwell, J. A., and Jones, T. J. 1974, *Ap. J.*, 191, 675.
Habing, H. J., Olnon, F. M., Winnberg, A., Matthews, H. E., and Baud, B. 1983, *Astr. Ap.*, 128, 230.
Harvey, P. M., Bechis, K. B., Wilson, W. J., and Ball, J. A. 1974, *Ap. J. Suppl.*, 27, 331.
Herman, J. 1983, Ph.D. thesis, University of Leiden.
Iben, I. Jr. 1981, in *Effects of Mass Loss on Stellar Evolution*, ed. C. Chiosi and R. Stalio (Dordrecht: Reidel), p. 373.
Jewell, P. R., Webber, J. C., and Snyder, L. E. 1980, *Ap. J. (Letters)*, 242, L29.
Johansson, L. E. B., Andersson, C., Goss, W. M., and Winnberg, A. 1977, *Astr. Ap. Suppl.*, 28, 199.
Jones, T. J., Ashley, M., Hyland, A. R., and Ruelas-Mayorga, A. 1981, *M.N.R.A.S.*, 197, 413.
Jones, T. J., Hyland, A. R., Caswell, J. L., and Gatley, I. 1982, *Ap. J.*, 253, 208.
Jones, T. J., Hyland, A. R., and Gatley, I. 1983, *Ap. J.*, 273, 660.
Jones, T. J., Hyland, A. R., Wood, P. R., and Gatley, I. 1983, *Ap. J.*, 273, 669.
Kwan, J., and Scoville, N. Z. 1976, *Ap. J.*, 209, 102.
Merrill, K. M. 1977, in *IAU Colloquium 42, The Interaction of Variable Stars with Their Environment*, ed. R. Kippenhahn, J. Rahe, and W. Strohmeier (Bamberg: Reimers-Sternwarte), p. 446.
Nguyen-Q-Rieu, Laury-Micoloutaut, C., Winnberg, A., and Schultz, G. V. 1979, *Astr. Ap.*, 75, 352.
Olnon, F. M., Baud, B., Habing, H. J., de Jong, T., Harris, S., and Pottasch, S. R. 1984, *Ap. J. (Letters)*, 278, L41.
Olnon, F. M., Walterbos, R. A. M., Habing, H. J., Matthews, H. E., Winnberg, A., Brezinska, H., and Baud, B. 1981, *Ap. J. (Letters)*, 245, L103.
Paczynski, B. 1970, *Acta Astr.*, 20, 47.
Werner, M. W., Beckwith, S., Gatley, I., Sellgren, K., and Berriman, G. 1980, *Ap. J.*, 239, 540.

B. Baud: Department of Space Research, University of Groningen, P.O. Box 800, 9700 AV Groningen, The Netherlands

A. F. Bentley: Department of Natural Sciences, Eastern Montana College, Billings, MT 59101

A. I. Sargent: Owens Valley Radio Observatory, California Institute of Technology 320-47, Pasadena, CA 91125

M. W. Werner: NASA-Ames Research Center, MS 245-6, Moffett Field, CA 94305

INFRARED OBSERVATIONS OF THE EARLY UNIVERSE

Alan F. Bentley
Department of Physical Sciences
Eastern Montana College
Billings, Montana

Abstract: The possibilities for making infrared observations of great scientific interest from above the Earth's atmosphere are discussed. It is shown that a telescope system like the Large Aperture Infrared Telescope System (LAIRTS), now undergoing development by the Air Force should be able to make certain unique observations which are beyond the capabilities of presently existing telescopes. These observations include galaxies in the process of formation in the early Universe, and searches for brown dwarf components of galactic halos.

INTRODUCTION

The latter half of the 20th century has seen the introduction of a large number of new techniques in observational astronomy, a revolution which continues today. The revolution has opened wide the entire electromagnetic spectrum for astronomical observations. Visual observations, utilizing photographic and photoelectric methods developed during the late 19th and early 20th centuries, are being complemented by ground-based radio and infrared observations; and satellite observatories operating at ultraviolet, x-ray, and gamma-ray frequencies are now realities. Our knowledge of the universe has also been substantially enhanced by high altitude observations at non-optical frequencies from aircraft, balloons, and sub-orbital rocket flights. In 1983 the Infrared Astronomy Satellite (IRAS) completed a high sensitivity survey over 95% of the entire sky, demonstrating the feasibility of making long-term infrared observations from space.

A new instrument conceived and being developed by a group at the Air Force Geophysical Laboratory (AFGL) in Massachusetts is the Large Aperture Infrared

Telescope System (LAIRTS). As envisioned, it will provide man with the next significant step forward in infrared observational capability. LAIRTS is to be launched above Earth's atmosphere, with the entire telescope cooled to ≤25K. Its major advantage over ground-based infrared telescopes will be its sensitivity, which depends on its cooled optics, and its location above the absorbing and emitting atmosphere. For observations of extended sources, and for mapping of pre-selected regions of space, LAIRTS will be fitted with an infrared imaging camera, making possible high sensitivity measurements at high spatial and medium spectral resolution. Certain observations, to be discussed herein, cannot be made at all by presently existing telescope systems, nor by others expected to become operational in the near future, such as the Hubble Space Telescope. LAIRTS will thus be an important, and presently unique, tool for making these types of observations.

LAIRTS IMAGING CAMERA

Sensor Description

The LAIRTS telescope design is a four mirror off-axis folded Schmidt, with no obscurations or spiders. The primary mirror is a 32" x 22" ellipse, with 3570 cm^2 collecting area. The optical system is diffraction limited for all $\lambda > 5$ μm.

A dichroic beamsplitter reflects 70% or more of $\mu <$ 30 μm radiation toward the three-mirror camera system, which then re-images the telescope field onto a detector array. The array consists of four 64 x 64 Si:As direct readout mosaics, arranged in a square. The field of view (FOV) for each pixel is an area on the sky 11 arcsec x 11 arcsec square, with 12 arcsec center-to-center distance between adjacent pixels. Adjacent 64 x 64 mosaics are separated by 48 arcsec, so that the total array covers a field 26.4 arc-minutes square.

Sensitivity

The sensitivity of the LAIRTS Imaging Camera is expected to be background limited by zodiacal emission (ZE). A model for the ZE, adopted from the SIRTF Interim Report (1978), was used to calculate flux

density from the ZE which the LAIRTS camera will detect at selected wavelengths. The results are shown in Table 1. These estimates agree reasonably well with ZE brightness observations made by IRAS at 12 and 25 μm in the direction of the ecliptic pole (Hauser et al., 1984).

Table 1. Zodiacal Emission

λ(μm)	Flux Density (mJy)
5	7.6
10	57
20	38

The noise equivalent power (NEP) for each element of an array detector is given by Lamb et al. (1984) as

$$NEP = E_\lambda \frac{1}{\eta} [2(\eta\Phi+\phi)]^{1/2} WHz^{-1/2} \quad (1)$$

where E_λ = photon energy

η = quantum efficiency

Φ = photon flux (photons/sec)

ϕ = dark current (electrons/sec)

Since the camera is expected to be background limited by the photon flux from the ZE, its NEP may then be calculated from

$$NEP \simeq E_\lambda \left[\frac{2\Phi}{\eta}\right]^{1/2} WHz^{-1/2} \quad (2)$$

where $\eta = 0.3$.

The 1σ sensitivity for an integration time $t_i = 1$ second is then

$$1\sigma \text{ sensitivity} = \frac{NEP}{\Sigma A_c} W\ cm^{-2} \quad (3)$$

where A_c = collector area = 3570 cm^2

Σ = system transmission due to optical losses

= 0.49 = $(0.98)^7(0.80)(0.70)$

[7 mirrors][filter][dichroic]

Using equations (2) and (3) the noise equivalent flux densities (NEFD's) of the camera for detection of both point and extended sources were calculated for selected wavelengths and spectral bandwidths. The result of these calculations are presented in Tables 2 and 3.

Table 2. NEFD of Imaging Camera for point source

(t_i = 1 second)

λ(μm)	$\Delta\lambda = 0.1\lambda$	$\Delta\lambda = 0.5\lambda$
5	440 μJy	200 μJy
10	1200 μJy	540 μJy
20	980 μJy	440 μJy

Table 3. NEFD of Imaging Camera for extended source

(t_i = 1 second)

λ(μm)	$\Delta\lambda = 0.1\lambda$	$\Delta\lambda = 0.5\lambda$
5	3.6 μJy/sq-arcsec	1.7 μJy/sq-arcsec
10	9.9 μJy/sq-arcsec	4.5 μJy/sq-arcsec
20	8.1 μJy/sq-arcsec	3.6 μJy/sq-arcsec

UNIQUE OBSERVATIONS

Objects of High Redshift

All astrophysical sources at great distances exhibit doppler-shifted spectra, indicating velocities of recession proportional to their distance. The observed wavelengths of radiation are shifted toward the red from the emitted (or rest) wavelengths. The corresponding cosmological redshift, Z, is defined in terms of the observed wavelength, λ', and the emitted wavelength, λ:

$$Z = \frac{\lambda' - \lambda}{\lambda} = \frac{\Delta\lambda}{\lambda}$$

The relationship between recession velocity, v, and redshift, Z, is:

$$Z = \left[\frac{1+v/c}{1-v/c}\right]^{1/2} - 1$$

It follows that observed energy distributions from distant sources are also redshifted. Contributions to the energy distribution redshift arise from 3 effects:

(1) The photon energy decreases

$$E_\nu' = \frac{E_\nu}{1+Z}$$

(2) A redshifted frequency interval becomes smaller

$$\Delta\nu' = \frac{\Delta\nu}{1+Z}$$

(3) The rate of photon emission decreases due to time dilation

$$\Delta_t' = \frac{\Delta_t}{\left[1 - \frac{v^2}{c^2}\right]^{1/2}}$$

The net result of these effects on the energy distribution is to decrease the observed flux density according to the relation

$$F_\nu' = KF_\nu W\ M^{-2}Hz\text{-}1$$

where

$$K = \left[1 - \frac{v^2}{c^2}\right]^{1/2} = \frac{2(1+Z)}{(1+Z)^2+1}$$

Values of K and recession velocities, V, for selected redshifts, Z, are given in Table 4.

Table 4. Values of K and V for Selected Values of Z

Z	V	K
0.3	0.257c	0.967
1.0	0.600c	0.800
2.0	0.800c	0.600
5.0	0.946c	0.324
10	0.984c	0.180
20	0.9955c	0.0950
100	0.9998c	0.0198

Giant elliptical galaxies are among the brightest visible objects known, making them among the easiest objects of high redshift to detect. A model galaxy was constructed based on the energy distribution discussed by Grasdalen (1980). The photometry, colors, and absolute K magnitudes published by Lebofsky (1980) were used to set an absolute scale for Grasdalen's energy distribution. The absolute visual magnitude of the model is $M_v = -23.1$. The apparent visual magnitude is then $m_v = 0.0$ at a distance of 0.41 Mpc, too close for an object to exhibit a measurable cosmological redshift. Spectral energy flux densities were then calculated for the model galaxy at selected values of the redshift, Z, including effects of the inverse-square law for radiant emission by point sources. At distances corresponding to $Z > 1.0$, all galaxies will appear as point sources in the field of the LAIRTS imaging camera. No model for galaxy evolution was adopted, and no contribution due to a possible non-zero value for the cosmological deceleration parameter (q_0) was included. The resulting expected flux densities for giant elliptical galaxies at various redshifts are given in Table 5. An examination of the table shows that the wavelength of peak emission is shifted continually red-ward for increasing Z.

The model predicts that a normal giant elliptical galaxy observed at $Z \simeq 5$ will exhibit a peak flux density of $\simeq$55μJy at 10 μm. With an NEFD of 540 μJy for 1 second integration (and $\Delta\lambda = 5$μm), a 40-minute integration time would be required to obtain a signal/noise ratio of 5. For $Z = 10$ the peak emission is near 20 μm, with a value of $\simeq$28 μJy. In this case,

Table 5. Expected Flux Densities for Giant Elliptical Galaxies at Various Redshifts (Z)

Z = 0		Z = 0.3		Z = 1.0		Z = 2.0		Z = 5.0		Z = 10		Z = 20		Z = 100	
(μm)	F_ν(μJy)	(μm)	F_ν(μJy)	(μm)	F_ν(μJy)	(μm)	F_ν(μJy)	(μm)	F_ν(μJy)	(μm)	F_ν(μJy)	(μm)	F_ν(μJy)	(μm)	F_ν(μJy)
0.40	728	0.52	112	0.80	17.1	1.20	7.2	2.40	2.8	4.40	1.4	8.40	0.737	40.0	0.152
0.42	968	0.55	149	0.84	22.7	1.26	9.6	2.52	3.7	4.62	1.9	8.82	0.981	42.4	0.202
0.45	1514	0.59	233	0.90	35.5	1.35	15.0	2.70	5.8	4.95	3.0	9.45	1.53	45.5	0.316
0.50	2353	0.65	362	1.00	55.2	1.50	23.3	3.00	9.0	5.50	4.6	10.5	2.38	50.5	0.492
0.55	2981	0.72	459	1.10	69.9	1.65	29.5	3.30	11.4	6.05	5.8	11.6	3.02	55.6	0.623
0.60	3548	0.78	546	1.20	83.2	1.80	35.1	3.60	13.6	6.60	7.0	12.6	3.59	60.6	0.742
0.70	4829	0.91	744	1.40	113	2.10	47.8	4.20	18.5	7.70	9.5	14.7	4.89	70.7	1.01
1.00	8584	1.30	1320	2.00	201	3.00	85.0	6.00	32.9	11.0	16.8	21.0	8.70	101	1.79
1.25	11680	1.63	1800	2.50	274	3.75	116	7.50	44.7	13.8	22.9	26.3	11.8	126	2.44
1.60	14520	2.08	2240	3.20	341	4.80	144	9.60	55.6	17.6	28.4	33.6	14.7	162	3.04
1.70	14280	2.21	2200	3.40	335	5.10	141	10.2	54.7	18.7	28.0	35.7	14.5	172	2.99
2.30	10890	2.99	1680	4.60	255	6.90	108	13.8	41.7	25.3	21.3	48.3	11.0	232	2.28

a detection with S/N = 5 (and $\Delta\lambda$ = 5 μm) would need 146 minutes of integration time.

Primordial Galaxies

Of particular interest are galaxies with redshifts of Z ≃ 5-10. According to one view of the early universe, proposed by Zel'dovich (1973), galaxies were formed by condensation from initial mass perturbations the size of galaxy clusters or superclusters. Galaxies thus formed are expected to collapse at redshifts ≃5 or less, and no galaxies with Z substantially greater than 5 would be expected to be observed. A distinctly different scenario, due to Press and Schechter (1974), depicts galaxies being built up from smaller, globular cluster size units. In this case galaxies are expected to form much earlier, at Z's of 20 or greater.

According to at least some galaxy formation models (c.f. Kaufman 1976), galaxy birth should be accompanied by a burst of star formation, with a period of peak brightness lasting ≃2 x 10^7 years, during which the galaxy luminosity should be dominated by hot O and B star emission. This should make the spectral energy distribution bluer than our galaxy model of Table 5, and about a factor of 100 brighter. The predicted integration times to detect bright starburst primordial galaxies at various redshifts, with $\Delta\lambda$ = 0.1λ, and S/N > 10 are given in Table 6.

Table 6. t_i (sec) to Detect Primordial Galaxies; S/N > 10; $\Delta\lambda$ = 0.1λ

λ(μm)	z = 5	z = 10	z = 20
5	3	196	--
10	5	68	3700
20	-	14	147

Massive Galactic Halos

Recent dynamical evidence (Einasto et al., 1974; Bok 1983) suggests that our Galaxy contains ≃5 x $10^{11} M_\odot$ of invisible matter in an extensive halo (radius ≥ 60 kpc) surrounding the readily observed visible disc. Similar evidence for the existence of massive halos has been obtained for a number of external spiral galaxies (Roberts 1975; Rubin et al.,

1978). A list of these galaxies is presented in Table 7.

Table 7. Spiral Galaxies with Flat Rotational Curves

NGC 4378	NGC 1620	NGC 7664
NGC 4594	NGC 3145	NGC 2998
NGC 7217	NGC 801	NGC 3672
NGC 2590	NGC 7541	

There is at present no observational evidence to give us a clue as to the form or physical properties of these massive invisible halos (Bok 1983). Suppose, however, that such a halo was completely made of brown dwarf stars, those theoretical objects midway in size between Jupiter and the sun, not quite massive enough to ever have initiated nuclear reactions in their cores. These stars would be cool and would emit energy at infrared frequencies. A possible model for a brown dwarf galactic halo could have the following characteristics:

Halo Shape:	spherical
Halo Radius:	60 kpc
Halo Mass:	$5 \times 10^{11} M_{\odot}$
Brown Dwarf Radius:	$0.1\ R_{\odot}$
Brown Dwarf Mass:	$0.01\ M_{\odot}$
Total No. of Brown Dwarf Stars:	5×10^{13}
Distance to Spiral Galaxy:	30 Mpc

The diameter of a spiral galaxy the same size as the Milky Way (radius $\simeq$ 15 kpc) at a distance of 30 Mpc would subtend an angle of $\simeq$3.4 arc-minutes. A 60 kpc radius halo would then lie inside 20 arc-minutes, and would be included in the 26 x 26 arc-min field of the LAIRTS camera. Based on the model parameters listed above, the predicted flux densities which would need to be measured by the LAIRTS Imaging Camera are given in Table 8 for brown dwarfs of various temperatures. For convenience, the calculated system NEFD is also given. Note that brown dwarf halos down to temperatures of $\simeq$300 K can be observed at 10 μm with S/N $\simeq$10 in less than 5 minutes, provided the model is

basically accurate. Such observations will be important. Even null results will be scientifically interesting, since they will set certain limitations on the form and characteristics of the matter which makes up the massive invisible halos.

Table 8. Expected Flux Densities from Brown Dwarf Halos

(μJy/square-arcsecond)

(μm)	T=150K	T=300K	T=600K	T=1000K	NEFD*
5	1.0×10^{-4}	1.5	189	1350	3.6
10	0.48	5.9	71	220	9.9
20	.18	2.2	9.5	21	8.1

SUMMARY

The potential for making infrared observations of great scientific interest exists. Observations of galaxy formation in the early universe should be possible using LAIRTS, which is now under development by the Air Force Geophysical Laboratory. Observations of brown dwarf components of galactic halos is also shown to be a possibility with LAIRTS. The implementation of both of these observing programs will significantly expand our knowledge of the universe in which we live.

ACKNOWLEDGEMENTS

This research was sponsored by the Air Force Office of Scientific Research, Air Force Systems Command, USAF, under Grant Number AFOSR 85-0139. The U.S. Government is authorized to reproduce and distribute reprints for Governmental purposes notwithstanding any copyright notation thereon.

LITERATURE CITED

Bok, B.J. 1983. Astrophys. J., 273: 411.

Einasto, J., Kaasik, A., and Saar, E. 1974. Nature, 250: 309.

Grasdalen, G.L. 1980. In, IAU Symp. No. 92, "Objects of High Redshift," ed. G.O. Abell and P.J.E. Peebles, (Dordrecht, Holland: Reidel), p. 269.

Hauser, M.G., et al. 1984. Astrophys. J. (Letters), 278: L15.

Kaufman, M. 1976. Astrophys. and Space Sci. 40: 369.

Lamb, Gerald, et al. 1984. (Preprint). "Astronomical Applications of the New Goddard Si:Bi 16x16 Array Camera System."

Lebofsky, M.J. 1980. In, IAU Symp. No. 92, "Objects of High Redshift," ed. G.O. Abell and P.J.E. Peebles, (Dordrecht, Holland: Reidel), p. 257.

Press, W.H., and Schechter, P. 1974. Astrophys. J. 187: 425.

Roberts, M.S. 1975. In, "Galaxies and the Universe," ed. A. Sandage, M. Sandage, and J. Kristian (Chicago: University of Chicago Press), p. 309.

Rubin, V.C., Ford, W.K., and Thonnard, N. 1978. Astrophys. J. (Letters), 225: L107.

SIRTF, Interim Report. 1978, NASA Ames.

Zel'dovich, Ya. B., and Novikov, I.D. 1973. "Structure and Evolution of the Universe," (Moscow: Nauka).

THE ASTROPHYSICAL JOURNAL, 308:L63–L66, 1986 September 15
© 1986 The American Astronomical Society. All rights reserved. Printed in U.S.A.

THE NEON NOVA. II. CONDENSATION OF SILICATE GRAINS IN THE EJECTA OF NOVA VULPECULAE 1984 NUMBER 2

R. D. GEHRZ,[1] G. L. GRASDALEN,[2] M. GREENHOUSE,[2] J. A. HACKWELL,[3] T. HAYWARD,[2] AND A. F. BENTLEY[4]

Received 1986 May 23; accepted 1986 June 17

ABSTRACT

Infrared photometry of Nova Vulpeculae 1984 number 2 (NV2) from 2.3 to 19.5 μm during 1985 May 14 to 1986 March 31 shows that silicate grains had condensed and grown in the nova ejecta by 1985 August 23, 240 days after the eruption. A relative overabundance of oxygen in the nova shell seems indicated. Forbidden 12.8 μm [Ne II] emission was a factor of ≈ 41 above the continuum at a spectral resolution of $\lambda/\Delta\lambda = 67$ on day 240; the line persisted through day 461. The anomalous chemical composition of NV2's ejecta supports recent suggestions that ONeMg white dwarfs evolved from 8–12 $M_\odot$ progenitor stars are accreting matter in binary systems.

Subject headings: infrared: sources — stars: individual — stars: novae

I. INTRODUCTION

We report the discovery of the 10 and 20 μm silicate emission features in Nova Vulpeculae 1984 number 2 (NV2) and suggest that silicate grains have formed in the ejecta. The observations provide an estimate of the total mass of silicate grains condensed in the shell.

The observations reported here, together with our earlier discovery in NV2 of strong [Ne II] emission at 12.8 μm (Gehrz, Grasdalen, and Hackwell 1985; hereafter Paper I), confirm the presence of oxygen-neon-magnesium (ONeMg) white dwarfs accreting matter in binary systems. Such novae may be capable of contributing significant quantities of the interesting radioactive isotopes ^{22}Na and ^{26}Al to the interstellar medium (see, for example, Hillebrandt and Thielemann 1982 and Truran 1984). Meteoritic abundance anomalies suggest that these extinct isotopes, the by-products of a transient nucleosynthetic event such as a nova eruption, were injected into the primitive solar system during the early stages of its formation (Truran 1984).

II. OBSERVATIONS

Photometric and spectrophotometric observations (Table 1 and Figs. 1–3) were obtained with the Wyoming bolometer (Gehrz, Hackwell, and Jones 1974) and the $\lambda/\Delta\lambda = 67$ As:Si spectrophotometer (Gehrz *et al.* 1984) on the 234 cm Wyoming Infrared Telescope. Several apertures (5″ or 6.″8) and beam separations (10″–18″) were used; the measurements are independent of these parameters because NV2's shell is spatially unresolved. Most observations reported here were made with remote telephone links enabling observers to control the Wyoming telescope and its instrumentation from laboratories in Laramie, Wyoming, and Minneapolis, Minnesota.

III. INFRARED SILICATE EMISSION

Broad-band photometry and narrow-band spectrophotometry for 1985 August 23.4 show the presence of the 10 μm silicate emission feature (Fig. 2). The 20 μm silicate emission feature was present on August 23.4, but the 19.5 μm flux level on May 15.4 was consistent with the free-free continuum extrapolated from data at shorter wavelengths (Fig. 1).

Both silicate features should have been detectable over the free-free continuum on May 15.4 had they been present at the level measured in August (see Figs. 1–3). The data imply that the silicate emission features had increased in intensity by at least a factor of 2 between May 15.4 and August 23.4 due to grain condensation and growth.

An alternative source of the silicate emission could be the illumination after day 140 of a dust shell remnant of the mass-loss phase of the nova progenitor (see Bode and Evans 1983). This seems unlikely. First, the material would have to lie $\geq 3.6 \times 10^{17}$ cm from the binary system and would subtend an angular diameter $\geq 16''$. NV2 is unresolved by a 5″ beam at 10 μm. Second, the temperature for grains directly illuminated by starlight at this distance from a source with NV2's outburst luminosity of $\approx 10^5\ L_\odot$ (Paper I, erratum) will be ≤ 40 K. The observed grain temperature is 200–400 K on day 240 assuming that the 20 μm/10 μm opacity ratio for silicate grains lies between 0.3 and 1. We cannot entirely rule out the possibility that the progenitor's ejecta are anisotropically distributed and that very small dust grains lying along the line of sight of our beam are impulsively heated by hard photons (Desert, Boulanger, and Shore 1985).

[1] Astronomy Department, School of Physics and Astronomy, University of Minnesota.
[2] Wyoming Infrared Observatory, Department of Physics and Astronomy, University of Wyoming.
[3] Space Sciences Laboratory, The Aerospace Corporation, Los Angeles, California.
[4] Department of Physical Sciences, Eastern Montana College, Billings, Montana.

TABLE 1

PHOTOMETRY OF NOVA VULPECULAE 1984 NUMBER 2

λ (μm)	MAGNITUDE Day 140 (05/14/85)	Day 171 (06/13/85)	Day 230 (08/13/85)	Day 240 (08/23/85)	Day 294 (10/16/85)	Day 335 (11/26/85)	Day 382 (01/12/86)	Day 461 (03/31/86)
2.3	+7.29 ± 0.04	+7.42 ± 0.03	+7.86 ± 0.08	+8.11 ± 0.03	+8.30 ± 0.05	...	+8.62 ± 0.12	+8.90 ± 0.21
3.6	+6.09 ± 0.02	+6.22 ± 0.01	+7.04 ± 0.14	+6.87 ± 0.03	+6.63 ± 0.05	...	+6.93 ± 0.10	+6.59 ± 0.06
4.9	+5.71 ± 0.08	+5.61 ± 0.07	+6.00 ± 0.24	+6.34 ± 0.09	...	+6.91 ± 0.28	+7.03 ± 0.15	
8.7	+4.43 ± 0.20	+4.03 ± 0.09	+4.49 ± 0.33	+4.70 ± 0.16	+4.44 ± 0.27	...	+4.61 ± 0.23	+4.34 ± 0.14
10.0[a]	...	+3.07 ± 0.09	...	+2.99 ± 0.05	+3.15 ± 0.16	+3.28 ± 0.02	+3.38 ± 0.14	+3.28 ± 0.08
N[b]	+2.70 ± 0.07	+3.04 ± 0.05	+3.10 ± 0.08	+3.20 ± 0.06	+3.30 ± 0.04	+2.67 ± 0.08	+3.39 ± 0.08	+3.30 ± 0.12
11.4	+3.20 ± 0.23	+3.04 ± 0.10	+2.76 ± 0.28	+2.81 ± 0.03	+2.91 ± 0.08	+2.02 ± 0.32	+3.44 ± 0.20	+3.19 ± 0.16
12.6	+1.69 ± 0.07	+2.05 ± 0.04	+2.25 ± 0.14	+2.33 ± 0.08	+2.38 ± 0.06	+1.95 ± 0.11	+2.20 ± 0.10	+2.95 ± 0.18
Q[b]	+2.55 ± 0.29	+1.97 ± 0.25	+1.97 ± 0.25	≥ +1.75(3 σ)	+1.83 ± 0.33	...	+2.03 ± 0.20	+2.42 ± 0.14

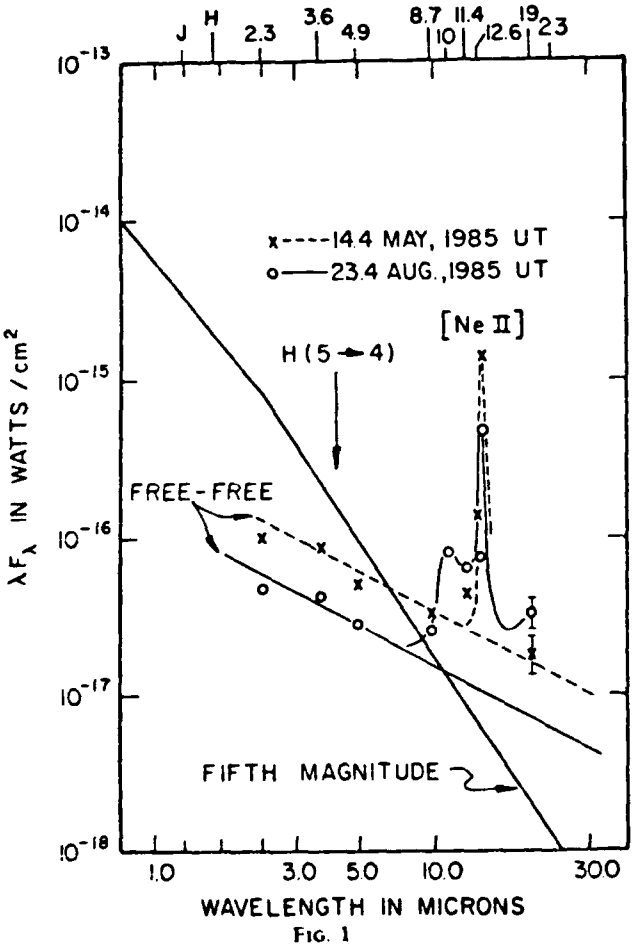

FIG. 1

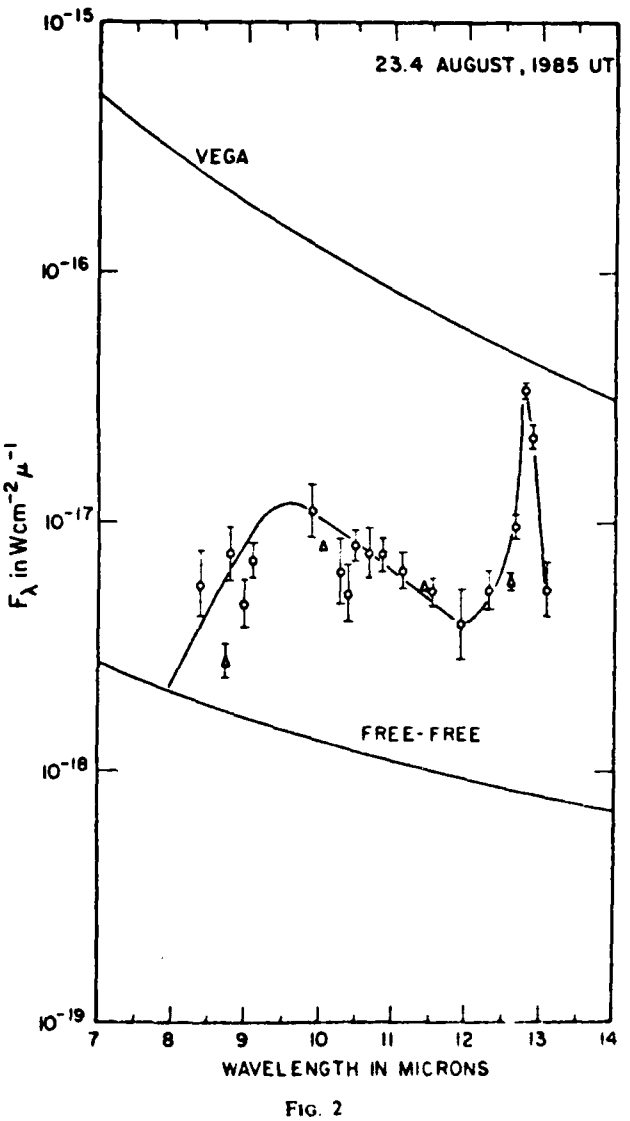

FIG. 2

FIG. 1.—Broad-band infrared energy distributions of NV2 before (*dashed line*) and after (*solid line*) the formation of circumstellar silicate grains. Narrow-band data are plotted for the 12.8 μm [Ne II] emission peak. Free-free lines indicate νF_ν = constant and have been normalized to photometry at λ ≥ 5 μm. Hydrogen (5 → 4) was present in the 3 μm band in 1985 May (Gehrz, Grasadalen, and Hackwell 1985). Error bars are smaller than the plotting symbols unless indicated. The neon line contaminates the 11.4 μm passband. Both the 10 and 20 μm silicate features are present in 1985 August.

FIG. 2.—Infrared spectrum of NV2 from 8 to 13.2 μm showing the 12.8 μm [Ne II] emission line and the 10 μm silicate emission feature. Triangles denote broad-band photometry. Vega denotes the zero magnitude calibration. Errors as indicated in legend for Fig. 1

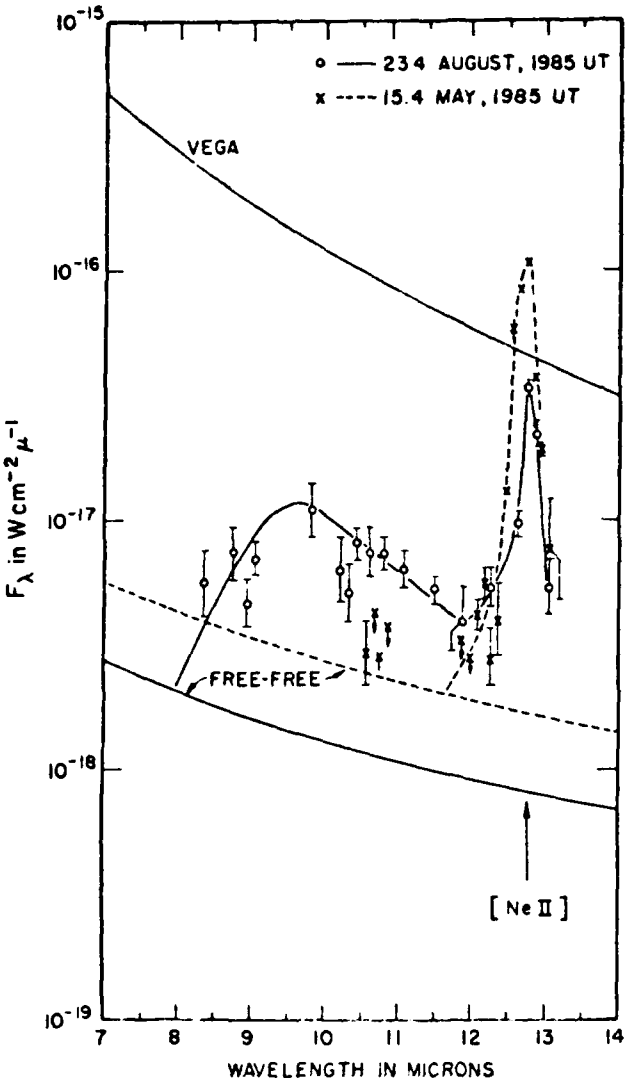

FIG. 3.—Comparison of the 10 μm spectra in 1985 May (*dashed line*) and August (*solid line*) showing that the silicate emission feature should have been detected well above the free-free continuum in May if it had been present at the level measured in August. Error bars are as indicated in the legend to Fig. 1.

IV. ABUNDANCES OF OXYGEN, NEON, AND GRAIN CONSTITUENTS

The formation of silicate grains suggests that the ejecta of NV2 are oxygen rich. It is believed (Hackwell 1971, 1972) that amorphous carbon and silicon carbide (SiC) grains form when C/O > 1, and that silicate grains condense when C/O < 1. Thus, the formation of carbon-rich (Gehrz *et al.* 1980*a*; Gehrz *et al.* 1980*b*) and SiC-rich (Gehrz *et al.* 1984) shells in novae presumably results from eruptions on carbon-oxygen (CO) white dwarfs evolved from low-mass stars.

In Paper I, we reported the discovery of forbidden 12.8 μm [Ne II] emission from NV2 with a peak intensity of ≈ 60 Jy in a 0.2 μm bandpass on 1985 May 15.4. We argued that neon was overabundant in the ejecta of NV2. C. H. Townes (private communication) confirmed the presence of the [Ne II] emission feature in 1985 June. The 12.8 μm [Ne II] emission feature had a peak intensity on August 23.4 of 18.5 Jy in a 0.2 μm bandpass. The decline in the line strength over the past year, considering the effects of shell expansion, suggests that excitation conditions have not changed appreciably. Our conclusion (Paper I) that the amount of neon in the form of [Ne II] alone must be at least solar abundance still obtains. Recent optical and ultraviolet spectroscopy of NV2 by the *IUE* nova team (S. G. Starrfield, private communication) reveals strong lines of Ne III and Ne IV ions as well. The infrared and *IUE* data demonstrate that neon is enhanced in the ejecta of NV2. Starrfield, Sparks, and Truran (1986) also report strong UV and optical emission from Mg II. Magnesium, predicted to be enhanced in the ejecta of ONeMg white dwarfs, is a primary constituent of the minerals which produce the 10 and 20 μm emission features.

We can estimate a lower limit to the total mass of the silicate material in the ejecta of NV2. The ratio of the flux observed from the 10 μm emission peak to the flux that would be emitted by an optically thick dust shell reradiating the outburst luminosity of ≈ 10^5 $L_\odot$ (Paper I, erratum) gives the mean shell silicate optical depth $\langle \tau_{10} \rangle$. The total mass M_{si} of silicates in the shell is

$$M_{si} \approx \pi R_s^2 \langle \tau_{10} \rangle / \kappa_{si},$$

where R_s is the shell radius and $\kappa \approx 3 \times 10^3$ cm^2 g^{-1} is the 10 μm silicate opacity. Assuming an expansion velocity of $V_0 \approx 1000$ km s^{-1} for the dust-forming component of the ejecta (Paper I), the shell should have attained a radius of 2.1×10^{15} cm by day 240, and an optically thick shell reradiating 10^5 $L_\odot$ on that day would have had a temperature of ≈ 600 K. The 10 μm flux predicted for such a shell compared to the intensity of the 10 μm silicate feature on day 240 gives $\langle \tau_{10} \rangle \approx 4 \times 10^{-3}$ and $M_{si} \approx 10^{-8}$ $M_\odot$. We note that the hydrogen mass associated with the silicate dust alone is ≈ 250 $M_{si} \approx 3 \times 10^{-6}$ $M_\odot$ if the Si abundance is normal. This is a fair fraction of the mass loss predicted for an explosion on the surface of an ONeMg white dwarf (Starrfield, Sparks, and Truran 1986) and, of course, excludes the mass associated with the high-velocity ejecta (see Paper I). Our calculations underestimate the value of $\langle \tau_{10} \rangle$ if the nova remnant subsided to the Eddington limit shortly after outburst (see Starrfield, Sparks, and Truran 1986) and if the nova remnant luminosity declined from the Eddington value thereafter. Thus, our estimate for M_{si} represents a lower limit.

V. DISCUSSION

We have argued that the silicate emission in NV2 indicates that grains nucleated and grew in the slow ejecta of NV2. Models of runaway nuclear explosions on the surface of an ONeMg white dwarf show that about half the ejected mass travels outward at velocities as low as 500–1000 km s^{-1}, which is consistent with the rather long time scale on which NV2 was observed to condense dust grains. Because silicates have a very low emissivity in the near-infrared, the late appearance of the shell is not unexpected and is generally

consistent with the proposition that the grains nucleated and grew after the ejecta in which the grains condensed passed the 1000 K radiation field point in the expanding shell (Gallagher 1977; Gehrz *et al.* 1980*a*; Gehrz *et al.* 1980*b*). Starrfield, Sparks, and Truran (1986) have suggested that the anomalous emission from the ejecta of NV2 can be explained by a runaway nuclear explosion on the surface of an ONeMg white dwarf. Law and Ritter (1983) suggested that some nova systems might contain ONeMg white dwarfs, and Nomoto (1983) has shown theoretically that these white dwarfs could be the remnants of 8–12 $M_{\odot}$ main-sequence progenitors.

The data presented in Paper I and by Starrfield, Sparks, and Truran (1986) establish that two of the crucial ingredients, neon and magnesium, are enhanced in the ejecta of NV2. Our discovery of the existence of silicate grains in the ejecta of NV2 shows that there is an enhancement of the third crucial ingredient of an ONeMg white dwarf, oxygen, in this nova.

We thank J. G. Cohen, J. S. Gallagher, F. C. Gillett, E. P. Ney, G. W. Preston, S. G. Starrfield, and J. W. Truran for stimulating discussions. C. H. Townes communicated his spectra of NV2 prior to publication. L. D. Chisholm, L. R. Shaw, C. Jaworowski, and T. Williams assisted with the observations and maintained the Wyoming systems. R. D. G. is supported by the Institute of Technology at Minnesota. Astronomy at Wyoming is funded by the National Science Foundation, the USAF, and the Department of Physics and Astronomy.

REFERENCES

Bode, M. F., and Evans, A. 1983, *Quart. J.R.A.S.*, **24**, 83.
Desert, F. X., Boulanger, F., and Shore, S. N. 1985, *Astr. Ap.*, submitted.
Gallagher, J. S. 1977, *A.J.*, **82**, 209.
Gehrz, R. D., Grasdalen, G. L., and Hackwell, J. A. 1985, *Ap. J. (Letters)*, **298**, L163 (Paper I); erratum 1986, *Ap. J. (Letters)*, **306**, L49.
Gehrz, R. D., Grasdalen, G. L., Hackwell, J. A., and Ney, E. P. 1980*a*, *Ap. J.*, **237**, 855.
Gehrz, R. D., Hackwell, J. H., Grasdalen, J. A., Ney, E. P., Neugebauer, G., and Sellgren, K. 1980*b*, *Ap. J.*, **239**, 570.
Gehrz, R. D., Hackwell, J. A., and Jones, T. W. 1974, *Ap. J.*, **191**, 675.
Gehrz, R. D., Ney, E. P., Grasdalen, G. L., Hackwell, J. A., and Thronson, H. A., Jr. 1984, *Ap. J.*, **281**, 303.
Hackwell, J. A. 1971, Ph.D. thesis, University College London.
———. 1972, *Astr. Ap.*, **21**, 232.
Hillebrandt, W., and Thielemann, F.-K. 1982, *Ap. J.*, **255**, 617.
Law, W. Y., and Ritter, H. 1983, *Astr. Ap.*, **123**, 33.
Nomoto, K. 1984, *Ap. J.*, **277**, 791.
Starrfield, S. G., Sparks, W. M., and Truran, J. W. 1986, *Ap. J. (Letters)*, **303**, L5.
Truran, J. W. 1984, *Ann. Rev. Nucl. Part. Sci.*, **34**, 53.

A. BENTLEY: Department of Physical Sciences, Eastern Montana College, Billings, MT 59101

R. D. GEHRZ: Astronomy Department, School of Physics and Astronomy, 116 Church Street, S. E., University of Minnesota, Minneapolis, MN 55455

G. L. GRASDALEN, M. A. GREENHOUSE, and T. HAYWARD: Wyoming Infrared Observatory, Department of Physics and Astronomy, University Station, Box 3905, University of Wyoming, Laramie, WY 82070

J. A. HACKWELL: Space Sciences Laboratory, The Aerospace Corporation, Mail Station MS-266, Post Office Box 92957, Los Angeles, CA 90009

A SEARCH FOR COOL COMPANIONS OF PLANETARY NEBULA NUCLEI

A. F. Bentley
Department of Physical Sciences
Eastern Montana College
Billings, Montana 59101

At present only a small number of planetary nebulae are known to possess binary nuclei. Since approximately 2/3 of main sequence stars are members of binary or multiple star systems, one might expect a large fraction of PN central stars to have gravitationally bound companions. Additionally, late-type stars are more numerous, and due to their low luminosities would be difficult to detect by visual observational methods at distances where PN are typically found ($\geq$1 kpc). (Only 5 known PN are thought to be nearer than 0.5 kpc). It is thus possible, and in our view probable, that a significant number of PN nuclei possess cool companions, hitherto undetected.

Since K and M stars emit a considerable fraction of their energy in the infrared, we calculated the feasibility of detecting them with the Wyoming InSb photometer, and found that such detections might be possible out to distances of $\simeq$2 kpc. To date 13 objects have been observed, including a sample of planetaries with known binary nuclei to test our hypothesis. The results are listed below.

Object	IR Excess	Remark	Object	IR Excess	Remark
NGC 7293	no		NGC 6905	no	
NGC 6853		no detection	NGC 6543	yes	known binary
NGC 246	yes	known binary	NGC 6572	yes	known binary
NGC 7008	?		NGC 6790	yes	
NGC 40	?		NGC 6210	yes	new binary?
NGC 6826	yes	new binary ?	A 63	yes	known binary
NGC 7009	yes	new binary ?			

The observations were made using standard infrared techniques in the J, H, K, and L bands. We used a 5 arc-sec aperture centered on the hot star. Any companion located within 2 arc-sec of the nucleus should have been within our beam. Thus, at a distance of 1 kpc, any binary system with a separation of $\leq$ 4000 A.U. should have been observed.

We caution that the results presented here are preliminary, and still subject to analysis. Specific models to fit the data are presently being constructed. We think that we may have detected 3 new binary nuclei, NGC 7009, NGC 6210, and NGC 6826. The interpretation for NGC 6790 is not clear. This work was supported by the U.S. Air Force Office of Scientific Research, the NSF, and University of Wyoming.

DRAFT COPY

CAN COSMIC RAY ENERGY BE TRANSFERRED AN ISOTROPICALLY TO AN ASTROPHYSICAL PLASMA?

A. F. Bentley

Department of Physical Sciences

Eastern Montana College

ABSTRACT

It is proposed that cosmic rays may be the primary source of the incremental energy required to produce the bipolar or elongated structure observed in many planetary nebulae. If their energy flux density is of the same order as that in the solar neighborhood, then in a few times 10^4 years the total energy carried by cosmic rays through a region in space occupied by an expanding planetary nebula is comparable to the kinetic energy of expansion of the nebula. Specific mechanisms for the transfer of cosmic ray energy to planetary nebulae are described.

I. Introduction

Morphological studies of planetary nebulae (PN) indicate that a significant fraction of extended PN exhibit noticeable elongation, or bipolar character. The long axes of these PN have been shown to lie preferentially parallel to the galactic equator (Melnick and Harwit, 1975), and to the interstellar magnetic field as determined from polarization measurements on stars in their vicinity (Grinin and Zverva, 1968). It is difficult to say why similar studies reported by Gurzadyan (1970) and Khromov and Kohoutek (1968) failed to show any correlation between the orientation of PN axes and the galactic equator, since few details of the investigations were presented in either case.

Kirkpatrick (1976) has proposed that the symmetries observed in PN are derived from associated symmetries present in the precursor stars, possibly related to rotation. Livio (1980) thinks that at least some observed symmetries can be explained by PN formation around close binary central stars. These mechanisms may very well operate in many instances, but if the alignment of PN axes of symmetry with the galactic magnetic field is true, then at least one mechanism in operation to produce these symmetries must be associated with the galactic magnetic field in some way, since there is no evidence that the axes of stellar rotation nor of binary orbits are not randomly oriented with respect to the galaxy (Slettebak 1949, van de Kamp 1958, Huang and Wade 1966, Huang 1967).

Cosmic rays (c.r.) are energetic charged particles (mostly protons) which naturally follow the interstellar magnetic field in their travels, as they gyrate in helical paths along magnetic field lines. It has been found that, through collective effects,

cosmic rays can stimulate the formation of Alfvén waves in the ISM through which they travel, and via this intermediary can deposit significant amounts of energy in the interstellar gas (Parker 1968, 1969; Meyer 1969; Wentzel 1972, 1974, 1977; Ginzburg et al. 1973).

In section II we show that if less than 1% of energy carried by cosmic rays is deposited in a PN, it is sufficient over a PN lifetime to account for the observed elongation of many PN. Calculations are presented in section III for two possible specific energy transfer mechanisms, followed by a brief discussion of boundary effects at the PN/ISM interface. We conclude in section IV that c.r. can ultimately be responsible for the observed axial symmetries of at least some PN.

II. Energy Considerations

The total kinetic energy of expansion of a "typical" PN is easily calculated. If we assume that a typical nebula contains a mass $m = 0.2\ M_\odot$ (Osterbrock 1974), and is expanding uniformly with a radial velocity $v_{ex} = 20$ km sec^{-1} (Osterbrock 1974), then the kinetic energy of expansion is

$$T_{ex} = \frac{1}{2} m v_{ex}^2 \simeq 8 \times 10^{44} \text{erg}$$

Suppose that we are able to couple the c.r. energy to a PN with some efficiency ε. Then the energy transferred from the c.r. to the nebula over some period of time τ can be expressed as

$$E(\tau) = \int_0^\tau \varepsilon\ F_c\ \sigma(t) dt$$

where F_c = cosmic ray flux

$\sigma(t)$ = effective nebular cross-section for c.r. interaction

For a circular geometric cross-section

$$\sigma(t) = \pi r^2(t) = \pi (v_{ex} t)^2$$

The energy which may be transferred during a period of time τ is then

$$E(\tau) = \int_0^\tau \varepsilon\ F_c\ \pi\ v_{ex}^2\ t^2 dt$$

If we assume that the coupling efficiency ε is independent of time, we obtain

$$E(\tau) = \frac{\pi}{3} \varepsilon\ F_c v_{ex}^2\ \tau^3$$

Using the c.r. flux, $F_c = 7 \times 10^{-3}$ erg cm^{-2}sec^{-1}, given by Allen (1973),

over a period of 3×10^4 years the energy transferred to a PN is

$$E(\tau = 3 \times 10^4 \text{yr}) = 2.5 \times 10^{46}\ \varepsilon \text{ erg}$$

which is significantly greater than the total kinetic energy of expansion of the nebula.

Starting with uniform spherically symmetric expansion as assumed above, how much additional kinetic energy is required to produce a PN with typical elongation (Khromov and Kohoutek 1968) of a/b = 1.5? If the average expansion velocity along the semi-minor axis b is 20 km sec^{-1}, then the average expansion velocity along the semi-major axis a must be 30 km sec^{-1}. We can create a crude model for the differential expansion by assuming that 90% of the nebular mass continues to expand at 20 km sec^{-1}, and 10% expands at 30 km sec^{-1}; the additional kinetic energy of expansion is

$$\Delta T_{ex} = \frac{1}{2}(0.1m)[(v_{ex} + \Delta v)^2 - v_{ex}^2] = 1 \times 10^{44} \text{ erg}$$

Thus the energy available from cosmic rays appears to be sufficient to account for the observed elongation of PN. The question remains as to whether such coupling can be shown to exist. We address this problem in the next section.

III. Coupling Between Cosmic Rays and Planetary Nebulae

One of the modern discoveries made concerning cosmic rays was that of collective effects (see e.g. the review by Wentzel, 1974). As c.r. stream through the galaxy along magnetic field lines, they are able collectively to generate hydromagnetic waves in the ISM which propagate through the gas at Alvén velocity

$$v_A = B\,(4\pi\,\rho_i)^{-1/2} \;;\; \rho_i = M_i n_i$$

= ion mass density

The Alfvén waves are low frequency transverse electromagnetic waves which travel along B parallel to the c.r. streaming direction. These waves, in turn, are capable of scattering the c.r. which produce them. In the process of being scattered, the c.r. transfer energy and momentum to the gas. This provides the basis by which c.r. energy can be transferred to PN. In the following we describe two mechanisms for c.r. energy transfer to PN, and comment upon a third.

A. Direct Interaction

Following Wentzel (1974), consider cosmic rays streaming down a c.r. density gradient through an ionized region (PN). We have seen in section II that the energy available from c.r. over $\tau = 3 \times 10^4$ yr is $2.5 \times 10^{46}\,\varepsilon$ erg, and the energy required for elongation of PN is 10^{44} erg. The efficiency of the energy transfer mechanism must then be $\varepsilon = .004$. The c.r. energy loss over a distance of one c.r. density scale height (L) is given as

$$\Delta E \simeq \frac{v_A}{\langle v \rangle}\, E$$

where $\langle v \rangle$ is the c.r. streaming velocity in the medium. For intercloud space Wentzel (1974) gives

$$\langle v \rangle = 55 + 110\left(\frac{P}{M_c}\right)^{1.5} \text{ km sec}^{-1}$$

so that for c.r. momentum $p \simeq M_c$ (~1 GeV c.r.), $\langle v \rangle \simeq 165$ km sec^{-1}. In a highly ionized region (e.g. PN), $\langle v \rangle$ is given by Wentzel as

$$\langle v \rangle = \frac{1}{3} \gamma v_A + 56 \left(\frac{100 \text{ pc}}{L}\right)^{1/2} \left(\frac{P}{M_c}\right)^{0.75} \text{ km sec}^{-1}$$

Using typical values suggested by Wentzel for the c.r. spectrum index $\gamma = 4.5$, the c.r. density scale height L = 100 pc, and $p \simeq M_c$, we find $\langle v \rangle \simeq 1.5 v_A + 56$ km sec^{-1}, placing a lower limit on the streaming velocity of 56 km sec^{-1} in a PN, with the exact value depending on the magnetic field strength B in the ionized region, through the Alfvén velocity v_A. The Alfvén velocity inside a typical PN ($n_i \simeq 10^3$ cm^{-3}) will be $v_A \simeq 0.2$ km sec^{-1} if the magnetic field strength is the same as the interstellar value ($B \simeq 3 \times 10^{-6}$ G), or $v_A \simeq 20$ km sec^{-1} if B should happen to be 2 orders of magnitude larger.

The time required for c.r. to stream down one c.r. density scale height L is $t \simeq L/\langle v \rangle \simeq 10^6$ yr, within a factor of 2, depending on $\langle v \rangle$. During the time $t \simeq 10^6$ yr c.r. will transfer $\Delta E = (v_A/\langle v \rangle)E$ erg to the medium through which they pass, and therefore, the energy transferred during a PN lifetime ($\tau \simeq 3 \times 10^4$ yr) is

$$\Delta E \simeq \frac{3 \times 10^4}{10^6} \frac{v_A}{\langle v \rangle} E \text{ erg}$$

$$\simeq 0.03 \frac{v_A}{\langle v \rangle} E \text{ erg}$$

In order for this mechanism to be viable we require

$$\varepsilon \simeq .004 \simeq .03 \frac{v_A}{\langle v \rangle}$$

Inside the ionized region we showed that $\langle v \rangle \simeq 1.5 v_A + 56$ km sec^{-1}. Combining this with the above, the Alfvén velocity in the PN must be

$$v_A \simeq 9 \text{ km sec}^{-1}$$

The corresponding magnetic field which must exist in the PN is then

$$B \geq 10^{-4} \text{ Gauss}$$

in order for substantial c.r. energy to be deposited in the nebula.

We have thus far implicitly assumed that the energy of cosmic ray heating is coverted to kinetic energy of expansion. Such is not necessarily the case, however, as we now show. For a typical electron kinetic temperature of $T_e \simeq 1 \times 10^4$ K, the speed of sound in a PN will be $c_o = (2N_e k T_e/\rho)^{\frac{1}{2}} \simeq 13$ km sec^{-1}. The theory of expansion of a gas cloud into vacuum as a result of gas pressure is discussed by Osterbrock (1974), the main result applicable here being that the bulk of the gas expands outward at a velocity slightly greater than the sound velocity, c_o. Thus, in order for expansion velocities on the order of 30 km sec^{-1} to be attained, the cosmic rays must heat the nebular gas to $T_e = \rho c_o^2/2N_e k \simeq 5 \times 10^4$ K. The radiative cooling rate in a typical PN ($T_e \sim 10^4$ K) is $\sim 3 \times 10^{-24} N_e^2$ erg/cm^3 - sec (Osterbrock, 1974). If ~10% of the nebular gas is heated by c.r. as discussed above, then the c.r. heating rate will be $\sim 1 \times 10^{-24} N_e^2 \epsilon$ erg/cm^3 - sec. The additional energy imput by c.r. will result in increased heating and cooling rates, with a maximum increase in the equilibrium kinetic temperature of ~900 K, for the case of $\epsilon = 1$. That is clearly insufficient to produce the required expansion velocities of ~30 km sec^{-1}. It therefore appears that most of the c.r. energy deposited in a PN by direct interaction will be converted to photons and radiated away rather than going into expansion.

B. Interstellar Medium as an Intermediary

We now consider a process whereby the ISM is heated by c.r. as they stream through it. The hot ionized portion of the ISM is then constrained to move along galactic magnetic field lines and upon encounter with a PN will preferentially heat those regions of the PN into which the galactic magnetic field lines lead, thus depositing the requisite kinetic energy in the PN at the right places to explain the observed elongations.

Savage and de Boer (1979) have reported observational evidence for the existence of a hot gaseous galactic corona which they conclude most likely has a kinetic temperature of $\sim 10^5$ K. We will now show that this can be explained in terms of c.r. heating.

As c.r. stream through the ISM some scattering occurs, and energy and momentum are deposited in the ISM. The scattering efficiency will depend on the c.r. streaming velocity $\langle v \rangle$ and the Alfvén velocity v_A in the medium. For intercloud space $\langle v \rangle \simeq 165$ km sec^{-1} (sec. II A.). The Alfvén velocity in the ISM is $v_A \simeq 38$ km sec^{-1} for $B = 3 \times 10^{-6}$G and $n_i \simeq 3 \times 10^{-2}$ cm^{-3} (Gómez-González and Guelin 1974). The energy transferred to the ISM during the time to traverse one scale height ($t \simeq L/\langle v \rangle \simeq 6 \times 10^5$ yr) is then

$$\Delta E = \frac{v_A}{\langle v \rangle} E \simeq 0.23E$$

Suppose the c.r. flux is more or less constant over the time t in a given region of space; then the energy per unit volume deposited by c.r. in the ISM in 6×10^5 yr will be

$$\frac{\Delta E}{V} = \frac{0.23 F_c}{\langle v \rangle} \simeq 10^{-10} \text{ erg cm}^{-3}$$

or, assuming equipartition of energy between electrons and ions, the energy transferred to each particle of the ISM is

$$\frac{\Delta E}{\text{particle}} = \frac{\Delta E}{2n_i V} = 1.6 \times 10^{-9} \text{ erg ion}^{-1}$$

This amount of energy per ion would imply a kinetic temperature for the ISM of ~8×10^6 K. This is consistent with the reported observations of the hot galactic corona at 10^5K, since it is expected that an equilibrium temperature for the ISM will be established by cooling through radiation in collisionally excited forbidden lines. Corresponding to a kinetic temperature of $T = 10^5$ K, the mean ion velocity will be

$$v_i = \left[\frac{3kT}{m_i}\right]^{1/2} \simeq 50 \text{ km sec}^{-1}$$

Now suppose that at some point in time a PN starts to form in a region of space which has been heated to ~10^5 K by cosmic rays. We note that the hot ISM ions will be constrained to move along interstellar magnetic field lines, since at $T \simeq 10^5$ K the gas pressure nkT is expected to be comparable to the magnetic pressure $B^2/8\pi$, rather than overwhelming it. The hot ISM ions will therefore approach a PN primarily along magnetic field lines.

Some <u>net</u> momentum associated with the c.r. streaming will have been transferred to the ISM, and subsequently to any PN encountered by the ISM ions. However, we must realize that the net momentum is the vector sum of momenta of nearly equal numbers of ions travelling in opposite directions along the magnetic field. The ISM can therefore interact with and deposit energy simultaneously in opposite sides of a PN. The deposited energy results in local heating and expansion of the nebular gas, producing the characteristic axial

symmetries observed in many PN.

Now consider the interaction of the ions of the ISM with those of a much more dense PN which they encounter. This will be characterized by Coulomb collisions, and the ion-ion interactions can be described in terms of an effective momentum transfer cross-section (see Appendix A)

$$\sigma_m = 4\pi \left[\frac{Z^2e^2}{m_i v_i^2}\right] \ln \left[\frac{\lambda_D m_i v_i^2}{Z^2 e^2}\right]$$

where Z = charge no. = 1 for hydrogen ions

$e = 4.8 \times 10^{-10}$ esu

$m_i = 1.67 \times 10^{-24}$ g

$v_i = 50 \times 10^5$ cm sec^{-1}

$\lambda_D = 22$ cm = Debye shielding length in PN (Appendix A)

We find $\sigma_m \simeq 8.5 \times 10^{-15}$ cm^2. The corresponding mean free path (mfp) for the ISM ions in the PN is

$$\text{mfp} \simeq \frac{1}{n_i \sigma_m} \simeq 10^{11} \text{ cm} \simeq 4 \times 10^{-8} \text{ pc}$$

where in this case n_i = ion density in PN.

Another approach to exmaining this interaction is to calculate the "slowing down" time, t_s, given by Spitzer (1956).

We find $t_s \simeq 1.3 \times 10^4$ sec, with the corresponding mfp for 50 km sec^{-1} ions

$$\text{mfp} \simeq v_i t_s \simeq 2 \times 10^{-8} \text{ pc}$$

in good agreement with the momentum cross-section calculation.

We see that the mfp for incident ions of the ISM is small with respect to the dimensions of the nebula at nearly every stage of expansion. Therefore the energy carried by the ISM must be completely transferred to the ions of the PN. It is important to realize that the c.r. energy thus depositied will result in purely local heating. For a mfp of $\sim 3 \times 10^{-8}$ pc calculated above, only $\sim 10^{-6}$ of the nebular mass will receive c.r. energy. The c.r. heating rate in the local regions of interaction will then be $\sim 1 \times 10^{-19} N_e^2 \varepsilon$ erg/cm^3 - sec. The kinetic energy of a 50 km sec^{-1} hydrogen ion is 2×10^{-11} erg, which gives an efficiency factor $\varepsilon = (0.23)(2 \times 10^{-11}/1.6 \times 10^{-9}) = .003$ for transfer of c.r. energy to the ISM and subsequently to PN. The c.r. local heating rate in PN is then $\sim 3 \times 10^{-22} N_e^2$ erg/cm^3 - sec, a factor of ~100 greater than the radiative cooling rate for a 10^4 K nebula. Most of the c.r. energy will therefore be available to be converted to kinetic energy of expansion, with very little of it lost to radiative cooling. The c.r. energy thus transferred during a typical PN lifetime (3×10^4 yr) will then be

$$E(\tau = 3 \times 10^4 \text{ yr}) = 2.5 \times 10^{46} \varepsilon \text{ erg (sec. II)}$$
$$= 7.5 \times 10^{43} \text{ erg}$$

Even though the calculations have been quite crude, we see that this result indicates reasonable agreement with the 10^{44} erg of additional energy required to explain PN elongation (sec. II).

The detailed scenario of PN interaction with the ISM over a PN lifetime is most likely quite complicated, and is not intended to be the subject of this paper. We note that as the outer layers of the PN expand as a result of the c.r. heating, the electron density N_e decreases, and the mfp therefore increases. In this way deeper layers of the PN are able to interact with the ISM ions, and it is reasonable

to expect that eventually a significant fraction of the PN mass will be subject to c.r. heating, the energy of which will be available for subsequent expansion.

C. Boundary Effects

It may be that the sharp boundaries which exist between the ISM and PN can contribute significantly to the energy transfer. The configuration of the interstellar magnetic field in the vicinity of PN is not known. However, it is well-known that the diffusion of a magnetic field through astrophysical plasmas, such as those we are considering here, is extremely slow, so much so as to effectively "freeze" the field into the plasma. The expanding motion of the PN plasma would presumably then carry any embedded magnetic field with it, since the gas pressure is several orders of magnitude larger than the magnetic pressure. This would produce some sort of kinking or bending of the magnetic field at the PN/ISM boundary. Theoretically, fluctuations in the galactic magnetic field with dimensions on the order of 10^{-5} pc will scatter cosmic rays (Wentzel 1974), thereby transferring energy from the c.r. to the surrounding medium. Whether variations in the magnetic field of this magnitude are present near PN/ISM boundaries is not known, but the possibility exists and could be important for transferring c.r. energy to PN.

IV. Summary

Attempts to invoke magnetic fields (Gurzadyan 1962, 1970; Woyk 1968) in direct interaction with planetary nebulae have not been fruitful (Kahn 1968; Woltjer 1968; Menzel 1968). Casting the galactic magnetic field in an accessory role, as proposed here, seems to be more promising. Cosmic rays of 1 GeV or more have been shown to carry sufficient energy to supply an expanding PN with the additional energy required to produce the observed elongations. Collective effects from cosmic ray theory have been used to explain how energy may be transferred from the cosmic rays to the PN. It seems that sufficient energy to explain the observations may be gained by the PN from interaction with the interstellar medium which has been heated by c.r., although other possibilities are not ruled out. The role which boundary effects might play remains to be considered in more detail. The existence of magnetic fields within PN of sufficient strength to make direct interaction of c.r. with nebular material a viable energy transfer mechanism remains yet to be disproved. Observations of Zeeman broadening in high-n hydrogen (radio recombination) lines might be used (Greve 1975, Troland and Heiles 1977, Greve and Pauls 1980) to detect or set an upper limit to magnetic field strength in PN.

Cosmic rays streaming along magnetic field lines may be the primary source of incremental energy for elongation of expanding planetary nebulae. This is consistent with our present understanding of cosmic ray physics, observations of the hot gaseous galactic corona, and alignment of planetary nebula axes along the galactic magnetic field.

Appendix A

DERIVATION OF THE MOMENTUM TRANSFER CROSS-SECTION

Consider a typical 2-particle collision with impact parameter b and scattering angle χ, specified by

$$\cot \frac{\chi}{2} = \frac{b m_i v_i^2}{q_i q_s}$$

where m_i, v_i, q_i are the mass, velocity, and charge of the incoming particle, and q_s is the charge of the scattering center. The Rutherford formula for the differential scattering cross-section takes the form (Gordon 1955)

$$\frac{d\sigma}{d\Omega} = \left[\frac{q_i q_s}{2 m_i v_i^2 \sin^2 \frac{\chi}{2}}\right]^2$$

The total cross-section is then

$$\sigma = \int_0^{\pi} \frac{d\sigma}{d\Omega} \, 2\pi \sin \chi d\chi$$

The fractional change in momentum along the forward direction will be proportional to $(1-\cos\chi)$. This leads us to define a momentum transfer cross-section, σ_m, as follows

$$\sigma_m = \int_{\chi = \chi_{min}}^{\pi} (1 - \cos \chi) \left(\frac{d\sigma}{d\Omega}\right) 2\pi \sin \chi d\chi$$

Using the Rutherford formula, this becomes

$$\sigma_m = \frac{\pi}{2} \left[\frac{q_i q_s}{m_i v_i^2}\right]^2 \int_{\chi_{min}}^{\pi} \frac{\sin\chi \, (1 - \cos \chi)}{\sin^4 \frac{\chi}{2}} \, d\chi$$

By trigonometric manipulation this can be put in the form

$$\sigma_m = 4\pi \left[\frac{q_i q_s}{m_i v_i^2}\right]^2 \int_{\chi_{min}}^{\pi} \frac{\cos \chi/2}{\sin \chi/2} \, d(\chi/2)$$

The solution is obtained by letting $y = \sin \chi/2$, and the result is

$$\sigma_m = 4\pi \left[\frac{q_i q_s}{m_i v_i^2}\right]^2 \ln \Lambda$$

$$\text{where } \Lambda \equiv \left| \frac{1}{\sin\left(\frac{\chi_{min}}{2}\right)} \right|$$

We note that

$$\lim_{\chi \to o} \Lambda = \left| \frac{2}{\chi_{min}} \right| \simeq \left| \cot \frac{\chi_{min}}{2} \right| = \left| \frac{b_{max} m_i v_i^2}{q_i q_s} \right|$$

In a plasma it seems reasonable to choose the maximum impact parameter, b_{max}, equal to the Debye shielding length, λ_D

$$b_{max} = \lambda_D = \left[\frac{kT_e}{4\pi n_e e^2}\right]^{1/2}$$

In a PN for which $T_e \simeq 10^4 K$ and $n_e \simeq 10^3$ cm^{-3}, we find $\lambda_D \simeq 22$cm. Letting $q_i = q_s = Ze$, the momentum transfer cross-section takes the final form

$$\sigma_m = 4\pi \left[\frac{Ze^2}{m_i v_i^2}\right]^2 \ln \left[\frac{\lambda_D m_i v_i^2}{Ze^2}\right]$$

References

Allen, C. W. 1973, Astrophysical Quantities, 3rd Ed., The Athlone Press, London.

Ginzburg, V. L., Ptuski, V. S., and Tsytovich, V. N. 1973, Ap. Space Sci., 21, 13.

Gómez-González, V. and Guelin, M. 1974, Astr. Ap., 32, 441.

Gordon, M. M. 1955, Am. J. Phys., 23, 247.

Greve, A. 1975, Solar Phys., 44, 371.

Greve, A. and Pauls, T. 1980, Astr. Ap., 82, 388.

Grinin, V. P. and Zverva, A. M. 1968, in IAU Symposium No. 34, Planetary Nebulae, p. 287, edited by D. E. Osterbrock and C. R. O'Dell, Reidel Publishing Co., Dordrecht, Holland.

Gurzadyan, G. A. 1962, The Magnetic Fields in Planetary Nebulae, in Vistas in Astronomy, 5, 40, Ed. by A. Beer, Pergamon Press, New York.

Gurzadyan, G. A. 1970, Planetary Nebulae, Reidel Publishing Co., Dordrecht, Holland.

Huang, S., and Wade, C., Jr. 1966, Ap. J., 143, 146.

Huang, S. 1967, Ap. J., 141, 985.

Huang, S. 1967, Ap. J., 150, 229.

Kahn, F. D. 1968, in IAU Symposium No. 34, Planetary Nebulae, p. 248, edited by D. E. Osterbrock and C. R. O'Dell, Reidel Publishing Co., Dordrecht, Holland.

Khromov, G. S. and Kohoutek, L. 1968, in IAU Symposium No. 34, Planetary Nebulae, p. 227, ed. by D. E. Osterbrock and C. R. O'Dell, Reidel Publishing Co., Dordrecht, Holland.

Kirkpatrick, R. C. 1976, Astrophys. Letters, 17, 7.

Livio, M. 1980, Ap. J. (Letters) (submitted).

Melnick, G. and Harwit, M. 1975, MNRAS, 171, 441.

Menzel, D. H. 1968, in IAU Symposium No. 34, Planetary Nebulae, p. 279, edited by D. E. Osterbrock and C. R. O'Dell, Reidel Publishing Co., Dordrecht, Holland.

Meyer, P. 1969, Ann. Rev. Astron. Ap., 7, 1.

Osterbrock, D. E. 1974, Astrophysics of Gaseous Nebulae, W. H. Freeman & Co., San Francisco.

Parker, E. N. 1968, in Nebulae and Interstellar Matter, ed. B. Middleburst, L. Aller, Chap. 14, U. Chicago Press.

Parker, E. N. 1969, Space Sci. Rev., 9, 651.

Savage, B. D. and de Boer, K. S. 1979, Ap. J. (Letters), 230, L77.

Slettebak, A. 1949, Ap. J., 110, 498.

Spitzer, L., Jr. 1956, Physics of Fully Ionized Gases, Interscience Publishers, New York.

Troland, T. H. and Heiles, C. 1977, Ap. J., 214, 703.

van de Kamp, P. 1958, Handbuch der Physik, 50, 202, ed. S. Flügge.

Wentzel, D. G. 1972, PASP, 84, 225.

Wentzel, D. G. 1974, Ann. Rev. Astron. Ap., 12, 71.

Wentzel, D. G. 1977, J. Geophys. Res., 82, 714.

Woltjer, L. 1968, in IAU Symposium No. 34, Planetary Nebulae, p. 292, edited by D. E. Osterbrock and C. R. O'Dell, Reidel Publishing Co., Dordrecht, Holland.

Woyk, E. 1968, in IAU Symposium No. 34, Planetary Nebulae, p. 275, edited by D. E. Osterbrock and C. R. O'Dell, Reidel Publishing Co., Dordrecht, Holland.